

SUZAKU OBSERVATIONS OF MODERATELY OBSCURED (COMPTON-THIN) ACTIVE GALACTIC NUCLEI SELECTED BY SWIFT/BAT HARD X-RAY SURVEY

TAIKI KAWAMURO¹, YOSHIHIRO UEDA¹, FUMIE TAZAKI², CLAUDIO RICCI^{3,4}, YUICHI TERASHIMA⁵

Draft version October 3, 2018

ABSTRACT

We report the results obtained by a systematic, broadband (0.5–150 keV) X-ray spectral analysis of moderately obscured (Compton-thin; $22 \leq \log N_{\text{H}} < 24$) active galactic nuclei (AGNs) observed with *Suzaku* and *Swift*/Burst Alert Telescope (BAT). Our sample consists of 45 local AGNs at $z < 0.1$ with $\log L_{14-195 \text{ keV}} > 42$ detected in the *Swift*/BAT 70-month survey, whose *Suzaku* archival data are available as of 2015 December. All spectra are uniformly fit with a baseline model composed of an absorbed cutoff power-law component, reflected emission accompanied by a narrow fluorescent iron-K α line from cold matter (torus), and scattered emission. Main results based on the above analysis are as follows. (1) The photon index is correlated with Eddington ratio, but not with luminosity or black hole mass. (2) The ratio of the iron-K α line to X-ray luminosity, a torus covering fraction indicator, shows significant anti-correlation with luminosity. (3) The averaged reflection strength derived from stacked spectra above 14 keV is larger in less luminous ($\log L_{10-50 \text{ keV}} \leq 43.3$; $R = 1.04^{+0.17}_{-0.19}$) or highly obscured AGNs ($\log N_{\text{H}} > 23$; $R = 1.03^{+0.15}_{-0.17}$) than in more luminous ($\log L_{10-50 \text{ keV}} > 43.3$; $R = 0.46^{+0.08}_{-0.09}$) or lightly obscured objects ($\log N_{\text{H}} \leq 23$; $R = 0.59^{+0.09}_{-0.10}$), respectively. (4) The [O IV] 25.89 μm line to X-ray luminosity ratio is significantly smaller in AGNs with lower soft X-ray scattering fractions, suggesting that the [O IV] 25.89 μm luminosity underestimates the intrinsic power of an AGN buried in a small opening-angle torus.

Subject headings: X-rays: galaxies – galaxies: active – galaxies: nuclei

1. INTRODUCTION

High-quality broadband X-ray spectral observations are essential to unveil the structure of active galactic nuclei (AGNs). The main X-ray continuum, which can be well approximated by a power law with an exponential cutoff, is thought to be Comptonized photons by a hot corona in the vicinity of the supermassive black hole (SMBH). This emission interacts with the surrounding cold matter, the putative “dusty torus” invoked by the AGN unified model (Antonucci 1993). When one observes the central engine through the torus (so-called type-2 or Compton-thin obscured AGNs; $22 \leq \log N_{\text{H}} < 24$), the spectrum shows a low energy cutoff due to photoelectric absorption. The torus also produces a reflected component, which is seen as a hump at ~ 30 keV, accompanied by a narrow iron-K α fluorescent line at $\simeq 6.4$ keV (e.g., George & Fabian 1991; Matt et al. 1991). The reflection component from the inner accretion disk with a relativistically broadened iron-K α line is often reported in type-1 AGNs (e.g., Tanaka et al. 1995; Nandra et al. 2007; Patrick et al. 2012), although it is more difficult to robustly confirm its existence in type-2 AGNs. It is because when we see an AGN through the torus with an edge-on view, the features are smeared out by the absorption and more significant broadening. A scattered

component by gas surrounding the torus is present, which is observed as a weak unabsorbed continuum in the soft X-ray band in obscured AGNs. The column density, the reflection strengths from the torus and disk, the equivalent width (EW) of an iron-K α line, and the scattering fraction all carry information on the distribution of surrounding matter.

Moderately obscured (Compton-thin) AGNs, defined as those with line-of-sight column densities of $22 \leq \log N_{\text{H}} < 24$, are the most abundant AGN population in the universe (Ueda et al. 2014; Aird et al. 2015; Ricci et al. 2015). Also, they are ideal targets to study gas distribution around the nucleus. Unlike the case of type-1 or unobscured AGNs ($\log N_{\text{H}} < 22$), the photoelectric absorption feature enables us to accurately measure N_{H} and to observe the scattered X-ray light thanks to the suppression of the direct component. Because effects by Compton scattering can be neglected, it is possible to accurately estimate the intrinsic X-ray luminosity in Compton-thin AGNs, whose measurement would become unavoidably somewhat model-dependent in Compton-thick AGNs ($\log N_{\text{H}} > 24$). Moreover, AGNs sometimes show time variation of the intrinsic luminosity and/or absorption (changing look AGNs; e.g., Risaliti et al. 2002; Guainazzi et al. 2005). In that case, they provide us with valuable information such as the locus and structure of the dusty torus.

Hard X-ray all-sky surveys performed with *INTEGRAL* IBIS/ISGRI and *Swift*/Burst Alert Telescope (BAT) give least biased AGN samples against the obscuration (e.g., Beckmann et al. 2009; Baumgartner et al. 2013), thanks to the high penetrating power of hard X-ray photons (> 10 keV). The *Suzaku* observatory (2005–2015; Mitsuda et al. 2007) was capable of simultaneously

¹ Department of Astronomy, Kyoto University, Kyoto 606-8502, Japan

² Mizusawa VLBI Observatory, National Astronomical Observatory of Japan, Osawa, Mitaka, Tokyo 181-8588, Japan

³ Instituto de Astrofísica, Facultad de Física, Pontificia Universidad Católica de Chile, Casilla 306, Santiago 22, Chile

⁴ EMBIGGEN anillo, Concepcion, Chile

⁵ Department of Physics, Ehime University, Matsuyama 790-8577, Japan

observing broadband X-ray spectra of AGNs, covering typically the 0.5–40 keV band. It achieved the best sensitivity at energies above 10 keV before *NuSTAR* as a pointing observatory (Harrison et al. 2013). The combination of *Suzaku* data and time averaged *Swift*/BAT spectra covering the 14–195 keV band is very powerful for studying the broadband X-ray spectra of local AGNs selected by *Swift*/BAT, allowing to improve the understanding of the absorbing and reprocessing material for individual obscured AGNs (e.g., Ueda et al. 2007; Winter et al. 2009b; Eguchi et al. 2009, 2011; Tazaki et al. 2011; Gandhi et al. 2013, 2015; Tanimoto et al. 2016)

This article is a summary paper reporting the data of essentially all local moderately-obsured AGNs observed with both *Suzaku* and *Swift*/BAT, except for a few objects whose data have been already intensively analyzed and published. The number of the targets is 45, all originally selected from the *Swift*/BAT 70-month catalog (Baumgartner et al. 2013). Among them, the *Suzaku* broadband spectra of 19 objects are reported here for the first time. Our main goal is to investigate the properties of matter around the nuclei through a uniform analysis of the broadband X-ray spectra. *Suzaku* summary papers for low luminosity AGNs and Compton-thick AGNs are presented by Kawamuro et al. (2016) and Tanimoto et al. (in prep.), respectively.

This paper is organized as follows. Section 2 describes the details of our sample and the overview of the data. We explain our procedure of the spectral analysis in Section 3. The results and discussion are presented in Section 4. Section 5 summarizes our findings. We adopt the cosmological parameters of $(H_0, \Omega_m, \Omega_{\lambda}) = (70 \text{ km s}^{-1} \text{ Mpc}^{-1}, 0.3, 0.7)$ when calculating a distance from a redshift. Unless otherwise noted, all errors are quoted at the 1σ confidence level for a single parameter of interest.

2. OBSERVATION AND DATA REDUCTION

2.1. Sample

Our sample of moderately-obsured (Compton-thin) AGNs consists of 45 *Swift*/BAT selected AGNs (Baumgartner et al. 2013) at $z < 0.1$ whose *Suzaku* archival data are available as of 2015 December. The advantage of this sample is its high-quality broadband X-ray spectra (0.5–150 keV) that allow us to robustly constrain the X-ray spectral features. As for the sample selection by N_{H} , we firstly check previous *Suzaku* papers that are complied by Ichikawa et al. (2012) and Fukazawa et al. (2011). For the rest of objects, we refer to the results with other satellites listed in Ichikawa et al. (2012) and Malizia et al. (2012). We exclude those that turned out to be not moderately-obsured ($22 \leq \log N_{\text{H}} < 24$) AGNs from our spectral analysis. As described in Section 4, time variation of N_{H} does not affect our sample selection. The hard X-ray luminosity averaged for 70 months is limited to $\log L_{14-195 \text{ keV}} > 42$, since objects with $\log L_{14-195 \text{ keV}} < 42$ are reported in Kawamuro et al. (2016). Radio-loud (e.g., PKS, 3C, or 4C sources) or blazar type objects, which possibly possess jets, are not included because of possible contamination of the X-ray emission due to the presence of a jet. Also, we exclude 3 bright objects with complex spectra, NGC 3227, NGC 3516, and NGC 4151, which have been intensively analyzed with different models such as relativistic reflection

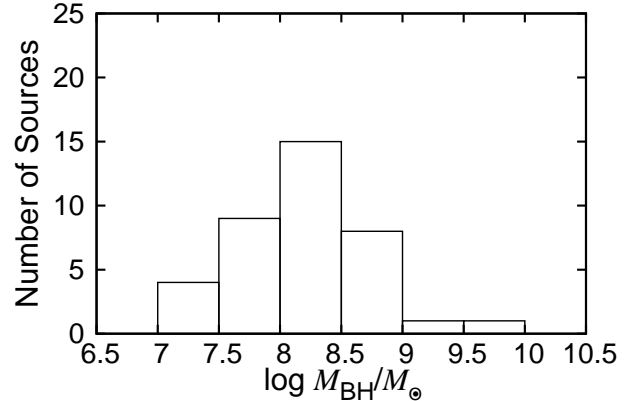


FIG. 1.— Distribution of black hole mass.

components from the inner disk, complex absorbers, and multiple power-law components (e.g., Patrick et al. 2012; Keck et al. 2015; Noda et al. 2014; Beuchert et al. 2015)

The basic information of the sample (i.e., galaxy name, position, redshift, distance, black hole mass M_{BH}) is listed in Table 1. The distances are the mean value available in the NASA/IPAC Extragalactic Database (NED), or calculated from the redshift when the distances are not available in the NED. We compile the black hole masses estimated by the gas dynamics around the SMBH, reverberation mapping, empirical formula using the broad-line width and luminosity in the optical band (e.g., H β and $\lambda 5100$), or relations of M_{BH} with bulge properties (e.g., velocity dispersion and K -band luminosity). When multiple SMBH masses are available for a single object, the mean value is taken. The M_{BH} distribution of our sample is represented in Figure 1. The mean and standard deviation of $\log(M_{\text{BH}}/M_{\odot})$, where M_{\odot} is the solar mass, is 8.1 ± 0.1 and 0.6 ± 0.1 , respectively. Throughout this paper, we adopt the 2–10 keV to bolometric correction factor of 20 (Vasudevan & Fabian 2009), which is applicable to AGNs with Eddington ratios of $\lambda_{\text{Edd}} < 0.1$. As described in Section 4.1, almost all of our objects show $\lambda_{\text{Edd}} < 0.1$. Adoption of the luminosity-dependent bolometric correction factor of Marconi et al. (2004) does not affect our main conclusions, except for the hard X-ray luminosity and Eddington ratio correlation (Section 4.1).

2.2. Data reduction

Suzaku carries the X-ray Imaging Spectrometers (XIS; Koyama et al. 2007) and the Hard X-ray Detector (HXD; Takahashi et al. 2007), sensitive to soft (< 10 keV) and hard X-ray photons (> 10 keV), respectively. Three of the four XISs are frontside-illuminated camera (FI-XISs; XIS-0, XIS-2, and XIS-3), and the other is a backside-illuminated one (BI-XIS; XIS-1). The HXD consists of the PIN diodes and GSO scintillators. Table 1 lists the IDs of the *Suzaku* observation data we analyze. If *Suzaku* observed an object on several occasions, we adopt the data with the longest exposure. For 2MASX J0350-5018, we utilize all observations because the exposure of a single observation is found to be too short for meaningful spectral analysis.

FTOOLS v6.15.1 and the *Suzaku* calibration database

released on 2015 Jan 5 are used for the data reduction. We reprocess the unfiltered XIS event data in the standard manner, as described in the ABC guide¹. The XIS source events are extracted from a circular region with radii of 1’–4’ depending on the flux, whereas the background is taken from an off-source region within the XIS field-of-view, where no other source is present. All the FI-XISs spectra available in each observation are combined into one to increase the signal-to-noise ratio. We generate the XIS response matrix and ancillary response files with `xisrmfgen` and `xissimarfgen` (Ishisaki et al. 2007), respectively. We bin the XIS spectra with minimum counts of 100 per bin. For HXD/PIN, we start with the “cleaned” event files provided by the *Suzaku*/HXD team. We make the background spectrum including the “tuned” non X-ray background model (Fukazawa et al. 2009) and the simulated Cosmic X-ray background spectrum based on Gruber et al. (1999). We basically use the HXD/PIN data in the 16–40 keV band for the spectral analysis. We further limit them to an energy band where the source signals are sufficiently higher than the uncertainty in the non X-ray background model: $\sim 3\%$ for exposures of less than 40 ksec and $\sim 1\%$ for longer exposures (Fukazawa et al. 2009).

3. BROADBAND SPECTRAL ANALYSIS

In addition to the *Suzaku* spectra, we also utilize the *Swift*/BAT spectra averaged for 70 months (Baumgartner et al. 2013). XSPEC (version 12.8.1.g) is used for the spectral analysis. We perform a simultaneous fit to the FI-XISs, BI-XIS, HXD/PIN, and *Swift*/BAT spectra, which cover the 1–10 keV, 0.5–8 keV, 16–40 keV, and 14–150 keV bands, respectively. The 1.7–1.9 keV XIS spectra are excluded to avoid the response uncertainties at the Si-K edge energy. Also, we do not use energy ranges where source photons are not significantly detected at 1σ . The cross-normalizations of the *Swift*/BAT and HXD/PIN spectra with respect to the FI-XISs spectrum are set to 1.0 and 1.16 (1.18) for the XIS (HXD) nominal position observation, respectively, whereas that of the BI-XIS one is left as a free parameter. By using the `phabs` model, we always consider the Galactic absorption ($N_{\text{H}}^{\text{Gal}}$), whose value is estimated from the H I map of Kalberla et al. (2005). Solar abundances given by Anders & Grevesse (1989) are assumed.

3.1. Baseline Model

To reproduce the broadband X-ray spectra covering the 0.5–150 keV band, we start with the following baseline model:

- `constant*zphabs*zpowerlw*zhighect`
`+constant*zhighect*zpowerlw+pexrav+zgauss.`

This model consists of an absorbed cutoff power law (transmitted component), a scattered component, and a reflection component from distant, cold matter accompanied by a narrow fluorescence iron-K α line. We fix the cutoff energy at 300 keV, a canonical value for nearby AGNs (Dadina 2008). Through the first `constant` model (N_{XIS}), we take into account possible time variation of the cutoff power-law component between the *Suzaku* and *Swift*/BAT spectra. The `zphabs` model is used to represent photoelectric absorption. The second term represents scattered emission of the primary X-ray component by gas located outside the torus. This unabsorbed component is assumed to have the same shape as the transmitted component with a fractional normalization of f_{scat} . The `pexrav` code (Magdziarz & Zdziarski 1995) reproduces reflected continuum emission, whose relative strength to the transmitted component is defined by $R = \Omega/2\pi$ (Ω is the solid angle of the reflector). The inclination angle to the reflector is fixed at 60° . To avoid unphysical fitting results, we impose an upper limit of $R = 2$, corresponding to the extreme case where the nucleus is covered by the reflector in all directions. The `zgauss` component represents an iron-K α fluorescent line, where the line width and energy is fixed at 20 eV and 6.4 keV, respectively. The width corresponds to a typical velocity dispersion of $\sim 2000 \text{ km s}^{-1}$ measured in local Seyfert galaxies with *Chandra*/HETGS by Shu et al. (2010). If the line energy is allowed to vary, the resultant value is consistent with 6.4 keV within the 99% confidence interval except for Fairall 51, Mrk 1498, and NGC 5506. For the three objects, we leave the line energy as a free parameter. We assume that the reflection components did not vary in accordance with the primary emission between the *Suzaku* and *Swift*/BAT observations, considering the large size of the reflector ($\sim 1 \text{ pc scale}$).

¹ <https://heasarc.gsfc.nasa.gov/docs/suzaku/analysis/abc/>

TABLE 1
INFORMATION OF TARGETS

Galaxy Name (1)	Swift ID (2)	RA. (3)	Dec. (4)	Redshift (5)	D (6)	$\log M_{\text{BH}}/M_{\odot}$ (7)	M_{BH} (8)	Ref.	<i>Suzaku</i> ID (9)	<i>Suzaku</i> Ref. (10)
2MASX J0216+5126	J0216.3+5128	34.124333	51.440194	0.0288	126.1	705006010	☆	
2MASX J0248+2630	J0249.1+2627	42.247199	26.510890	0.057997	259.3	704013010	☆	
2MASX J0318+6829	J0318.7+6828	49.579079	68.492062	0.090100	412.0	702075010	1	
2MASX J0350-5018	J0350.1-5019	57.599042	-50.309917	0.036492	160.6	8.8	1	701017010 [†]	2	
2MASX J0444+2813	J0444.1+2813	71.037542	28.216861	0.011268	38.6	7.4	2	703021010	☆	
2MASX J0505-2351	J0505.8-2351	76.440542	-23.853889	0.035041	154.1	7.5	1	701014010	2	
2MASX J0911+4528	J0911.2+4533	137.874863	45.468331	0.026782	117.1	7.5	1	703008010	☆	
2MASX J1200+0648	J1200.8+0650	180.241393	6.806423	0.036045	158.6	8.5	1	703009010	1	
Ark 347	J1204.5+2019	181.1236551	20.3162130	0.022445	97.8	8.1	1	705002010	☆	
ESO 103-035	J1838.4-6524	279.584750	-65.427556	0.013286	57.5	7.5	1,3	703031010	3	
ESO 263-G013	J1009.3-4250	152.450875	-42.811222	0.033537	147.3	8.0	4	702120010	1,4	
ESO 297-G018	J0138.6-4001	24.654833	-40.011417	0.025227	110.1	9.7	1	701015010	2	
ESO 506-G027	J1238.9-2720	189.727458	-27.307833	0.025024	109.2	8.6	1	702080010	1,5	
Fairall 49	J1836.9-5924	279.242875	-59.402389	0.020021	87.1	702118010	1,6,7	
Fairall 51	J1844.5-6221	281.224917	-62.364833	0.014178	45.9	8.0	5	708046010	8	
IC 4518A	J1457.8-4308	224.421583	-43.132111	0.016261	70.5	7.5	3	706012010	☆	
LEDA 170194	J1239.3-1611	189.72	-16.23	0.040000	161.5	8.9	1,3	703007010	☆	
MCG +04-48-002	J2028.5+2543	307.146083	25.733333	0.013900	60.2	7.1	4	702081010	1,5	
MCG -01-05-047	J0152.8-0329	28.204167	-3.446833	0.017197	68.5	7.6	4	704043010	☆	
MCG -02-08-014	J0252.7-0822	43.097481	-8.510413	0.016752	72.7	704045010	☆	
MCG -05-23-016	J0947.6-3057	146.917319	-30.948734	0.008486	36.6	7.4	1,3	700002010	1,9,10,11	
Mrk 1210	J0804.2+0507	121.0244092	5.1138450	0.013496	58.4	7.9	6	702111010	1,12	
Mrk 1498	J1628.1+5145	247.016937	51.775390	0.054700	244.0	8.6	1	701016010	1,2	
Mrk 18	J0902.0+6007	135.493323	60.151709	0.011088	47.9	7.5	1	705001010	☆	
Mrk 348	J0048.8+3155	12.1964225	31.9569681	0.015034	65.1	8.0	1	703029010	13	
Mrk 417	J1049.4+2258	162.378861	22.964555	0.032756	143.8	8.0	1	702078010	1,5	
Mrk 520	J2200.9+1032	330.174548	10.54972	0.026612	108.0	8.3	7	407014010	☆	
Mrk 915	J2236.7-1233	339.193768	-12.545162	0.024109	105.2	8.1	5	708029010	☆	
NGC 1052	J0241.3-0816	40.2699937	-8.2557642	0.005037	19.7	8.7	8	702058010	1,10,14	
NGC 1142	J0255.2-0011	43.8008169	-0.1835573	0.028847	126.3	9.2	1,3,4	701013010	1,2	
NGC 2110	J0552.2-0727	88.047420	-7.456212	0.007789	35.6	8.3	1	100024010	1,9,10,15	
NGC 235A	J0042.9-2332	10.720042	-23.541028	0.022229	96.8	8.8	1	708026010	☆	
NGC 3081	J0959.5-2248	149.873080	-22.826277	0.007976	26.5	7.7	1,4,9	703013010	1,16	
NGC 3431	J1051.2-1704A	162.812667	-17.008028	0.017522	76.1	707012010	☆	
NGC 4388	J1225.8+1240	186.444780	12.662086	0.008419	20.5	8.0	1,3,4,9	800017010	1,10,17	
NGC 4507	J1235.6-3954	188.9026308	-39.9092628	0.011801	51.0	8.0	1,3,4,9	702048010	1,18	
NGC 4992	J1309.2+1139	197.2733500	11.6341550	0.025137	109.7	8.4	1,3,4	701080010	1,4	
NGC 5252	J1338.2+0433	204.5665139	4.5425817	0.022975	83.6	8.9	1,3	707028010	☆	
NGC 526A	J0123.8-3504	20.9766408	-35.0655289	0.019097	83.0	8.0	1,5	705044010	☆	
NGC 5506	J1413.2-0312	213.3120500	-3.2075769	0.006181	23.8	7.5	1,3,4,9	701030020	1,3,10,11	
NGC 6300	J1717.1-6249	259.247792	-62.820556	0.003699	13.9	7.3	3,4	702049010	1	
NGC 7172	J2201.9-3152	330.5078800	-31.8696658	0.008683	33.9	8.0	1,3,4,9	703030010	1	
NGC 788	J0201.0-0648	30.2768639	-6.8155172	0.013603	58.9	8.2	1,3,4	703032010	☆	
UGC 03142	J0443.9+2856	70.944958	28.971917	0.021655	94.3	8.3	10	707032010	☆	
UGC 12741	J2341.8+3033	355.481083	30.581750	0.017445	76.4	704014010	☆	

NOTE. — (1) Galaxy name. (2) *Swift*/BAT name in the 70-month catalog (Baumgartner et al. 2013). (3)–(5) Position in units of degree and redshift taken from the NED. (6) Distance in units of Mpc. (7)–(8) Black hole mass and the reference. (9) Observation ID of the *Suzaku* data we analyze. (10) Paper already reporting the *Suzaku* spectral analysis.

References for black hole masses.

- (1) Winter et al. (2009a) (2) Vasudevan et al. (2010) (3) Panessa et al. (2015) (4) Khorunzhev et al. (2012) (5) Bennert et al. (2006) (6) Zhang et al. (2008) (7) Winter et al. (2010) (8) Dopita et al. (2015) (9) Diamond-Stanic & Rieke (2012) (10) Wang & Zhang (2007)

References for papers.

- (1) Fukazawa et al. (2009) (2) Eguchi et al. (2009) (3) Gofford et al. (2013) (4) Comastri et al. (2010) (5) Winter et al. (2009b) (6) Tripathi et al. (2013) (7) Lobban & Vaughan (2014) (8) Svoboda et al. (2015) (9) Reeves et al. (2007) (10) Miyazawa et al. (2009) (11) Patrick et al. (2012) (12) Matt et al. (2009) (13) Marchese et al. (2014) (14) Brenneman et al. (2009) (15) Rivers et al. (2014) (16) Eguchi et al. (2011) (17) Shirai et al. (2008) (18) Braito et al. (2013) (☆) The *Suzaku* spectra are reported for the first time in this paper.

†We also analyze the data, whose observation IDs are 701017020 and 701017030.

TABLE 2
CORRELATIONS

Y (1)	X (2)	Sample (3)	N (4)	$\rho(X, Y)$ (5)	$P(X, Y)$ (6)	a (7)	b (8)
$\log \lambda_{\text{Edd}}^{\text{BAT}}$	$\log L_{10-50 \text{ keV}}^{\text{BAT}}$	All	38	0.17	3.1×10^{-1}
Γ	$\log L_{10-50 \text{ keV}}^{\text{BAT}}$	All	45	-0.26	8.6×10^{-2}
$\log N_{\text{H}}$	$\log L_{10-50 \text{ keV}}^{\text{BAT}}$	All	45	0.08	5.9×10^{-1}
Γ	$\log \lambda_{\text{Edd}}^{\text{BAT}}$	All	38	0.41	9.7×10^{-3}	2.11 ± 0.01	0.20 ± 0.01
$\log N_{\text{H}}$	$\log \lambda_{\text{Edd}}^{\text{BAT}}$	All	38	-0.04	7.9×10^{-1}
Γ	$\log N_{\text{H}}$	All	45	-0.03	8.6×10^{-1}
$\log L_{\text{K}\alpha}$	$\log L_{10-50 \text{ keV}}^{\text{BAT}}$	All	45	0.89	4.1×10^{-16}	0.2 ± 1.8	0.94 ± 0.04
R	$\log L_{10-50 \text{ keV}}^{\text{BAT}}$	All	45	-0.29	5.6×10^{-2}
R	$\log(L_{\text{K}\alpha}/L_{10-50 \text{ keV}}^{\text{BAT}})$	All	45	0.38	1.0×10^{-2}
R	$\log N_{\text{H}}$	All	45	0.04	7.9×10^{-1}
$\log \lambda L_{\lambda 12\mu\text{m}}$	$\log L_{10-50 \text{ keV}}^{\text{BAT}}$	All	43	0.67	1.0×10^{-6}	3.7 ± 3.0	0.92 ± 0.07
$\log \lambda L_{\lambda 12\mu\text{m}}$	$\log L_{10-50 \text{ keV}}^{\text{BAT}}$	Nuc.	28	0.53	3.8×10^{-3}	3.8 ± 4.1	0.91 ± 0.10
$\log \lambda F_{\lambda 12\mu\text{m}}$	$\log F_{10-50 \text{ keV}}^{\text{BAT}}$	All	43	0.63	5.8×10^{-6}	0.9 ± 1.0	1.06 ± 0.09
$\log \lambda F_{\lambda 12\mu\text{m}}$	$\log F_{10-50 \text{ keV}}^{\text{BAT}}$	Nuc.	28	0.60	6.9×10^{-4}	1.8 ± 1.3	1.15 ± 0.13
$\log L_{[\text{O IV}]}$	$\log L_{10-50 \text{ keV}}^{\text{BAT}}$	All	33	0.10	5.8×10^{-1}	-7.8 ± 4.9	1.13 ± 0.12
$\log(L_{[\text{O IV}]}/L_{10-50 \text{ keV}}^{\text{BAT}})$	$\log f_{\text{scat}}$	All	32	0.35	4.9×10^{-2}	-2.25 ± 0.11	0.98 ± 0.07

NOTE. — (1) Y variable. (2) X variable. (3) Sample used for the fitting. Nucleus (Nuc.) corresponds to the sample whose $12 \mu\text{m}$ luminosities were measured at high spatial resolution. (4) Number of objects of the sample. (5) Spearman's Rank coefficient for the correlation. (6) Null hypothesis probability of obtaining no correlation. (7)-(8) Fitting parameters of $Y = a + bX$, which are derived for the correlations with the null hypothesis probabilities smaller than 5% except for the correlations of R , and that of the $[\text{O IV}]$ versus X-ray luminosity.

After fitting the spectra with the above baseline model, we systematically test if inclusion of other model components improves the fit. We adopt a new model if the improvement is found to be significant at a 99% confidence level (i.e., $\Delta\chi^2 < -6.64$ and < -9.21 , which correspond to the 99% limits of the χ^2 distribution with degrees of freedom of 1 and 2, respectively.). The additional model components we consider are as follows: (1) optically-thin thermal emission from the host galaxy (`apec` in XSPEC), (2) partial absorption of the cutoff power-law component (`zpcfabs`), (3) absorption of the reflection components (`zphabs`), by considering that emission from a large-scale reflector like a dusty torus (e.g., see Figure 2 of Ikeda et al. 2009) may be subject to absorption different from that in the line of sight, and (4) emission/absorption lines (`zgauss`) of He-like iron ions at 6.70 keV, H-like iron ions at 6.97 keV, iron-K β at 7.06 keV, and nickel-K α at 7.48 keV. The Compton shoulder of an iron-K α line is also considered, which is modelled by a gaussian (`zgauss`) at 6.31 keV (e.g., Matt 2002; Shirai et al. 2008). The line width (1σ) of these lines is set to 20 eV. Moreover, we systematically survey other emission or absorption lines (e.g., those of ultra fast outflow) at energies above 6.4 keV by adding a line component (`zgauss`) with two additional free parameters (line energy and normalization). We include lines if the improvement of χ^2 is larger than $\Delta\chi^2 = 9.21$. We also check the absorption lines reported by Tombesi et al. (2011), who analyzed *XMM-Newton* data, but we do not detect any of them in our *Suzaku* spectra at >99% confidence level. It would be because they are too weak or variable.

In the Appendix, Table A summarizes the results of the spectral analysis. We obtain good fits for all targets, which fulfill either $\chi^2/d.o.f < 1.2$ or null hypothesis probability larger than 1%. Figure A and Figure B show the unfolded spectra and best-fit models in the 0.5–150 keV and 4–9 keV bands, respectively. Table B lists the flux, absorption-corrected luminosity, Eddington ratio, and EW of the iron-K α line with respect to the total continuum. Here, we define the Eddington luminosity as $L_{\text{Edd}} = 1.26 \times 10^{38} (M_{\text{BH}}/M_{\odot})$ erg s $^{-1}$. The information of the detected emission/absorption lines is listed in Table C.

3.2. Relativistic Reflection Component from the Accretion Disk

We further examine whether the spectra statistically require relativistically blurred reflection component from the inner optically-thick accretion disk. For this purpose, we use the model `constant*kdblur*reflionx`, where `reflionx` calculates a reflected continuum and emission lines from an ionized disk (Ross & Fabian 2005) and `kdblur` reproduces relativistic effects in the vicinity of a SMBH. Compared with type-1 AGNs, this component, if any, would be more difficult to detect and characterize in type-2 AGNs because of the absorption and lower flux contribution in edge-on geometry. Thus, we minimize the number of the free parameters. Among the parameters of the `reflionx` model, the photon index (Γ) and normalization are liked to those of the primary cutoff power-law component in the baseline model. We assume two ionization parameters of the disk ($\xi = 10$ and 100). The parameters of the `kdblur` model are a radial emis-

sivity index q (emissivity $\propto r^{-q}$), inner and outer radii (r_{in} and r_{out}), and inclination angle (θ_{inc}). We allow r_{in} to vary within 1–100 r_g (r_g is the Gravitational radius); this upper limit is imposed to avoid strong coupling with the narrow iron line from distant matter. We fix q , r_{out} , and θ_{inc} at 3, 400 r_g , and 60°, respectively. Because the `reflionx` model does not have an explicit parameter of the reflection strength ($\Omega/2\pi$), we quantify it by multiplying the `constant` model. Its upper limit is set to 3.2×10^{-3} and 3.2×10^{-4} for $\xi = 10$ and 100, respectively, which reproduces the same 10–100 keV flux as the `pexrav` model with $\Omega/2\pi = 1$ for a photon index of 1.7. The disk reflection component is subject to the same (partial) absorption models as for the primary component. In summary, only the inner radius (r_{in}) and normalization (`constant`) are left as free parameters.

Adding the disk-reflection component to the best-fit models obtained in Section 3.1, we find that fits are significantly improved at >99% confidence level in four sources (2MASX J1200+0648, Fairall 49, NGC 526A, and NGC 6300). Their unfolded spectra that give a smaller χ^2 value between the assumptions of $\xi = 10$ or 100 are shown in Figure C. Except for NGC 6300, the disk-reflection component better improves the fit at energies below 10 keV than above 10 keV. That is, a broad iron-K α line feature is more essential to reproduce the spectra than the reflection hump at ~ 30 keV in the first three objects. Possible presence of an ionized-disk reflection component in 2MASX J1200+648 and NGC 6300 is suggested here for the first time, while it was reported for Fairall 49 by Iwasawa et al. (2004), consistent with our result. Nandra et al. (2007) analyzed the *XMM-Newton* spectra of NGC 526A and found that the relativistic reflection can well reproduce the spectra but is indistinguishable from absorption models in terms of statistics.

Table D summarizes the resultant parameters of the disk-reflection component. For convenience, the normalization factor is converted into equivalent reflection strength in units of $\Omega/2\pi$. The fraction of these AGNs (4 out of 45) should be regarded as a conservative lower limit, because of the small ranges of parameters we have investigated and of the limitation in the spectral quality. We leave detailed discussion on the relativistic reflection components in obscured AGNs for future studies.

4. RESULTS AND DISCUSSION

In this section, we summarize X-ray properties of our sample obtained from the spectral analysis described in Section 3.1, and investigate correlations among them. We always refer to the results with the best-fit model without the relativistic disk-reflection component (Section 3.1) for all targets. Inclusion of the disk-reflection components little affects the other spectral parameters for the four objects reported in Section 3.2. Then we also compare them with the MIR properties (12 μm and [O IV] 25.89 μm , hereafter [O IV], luminosity). To statistically quantify the correlation strength between two variables (X, Y), we calculate the Spearman's rank coefficients $\rho(X, Y)$ and standard Student's t-null significance levels $P(X, Y)$. To derive a linear regression line with a form of $Y = a + bX$, we adopt the ordinary least-square (OLS) bisector method (Isobe et al. 1990) for luminosity-luminosity correlations, or the least chi-square method for the others, unless otherwise noted. Table 2 gives the

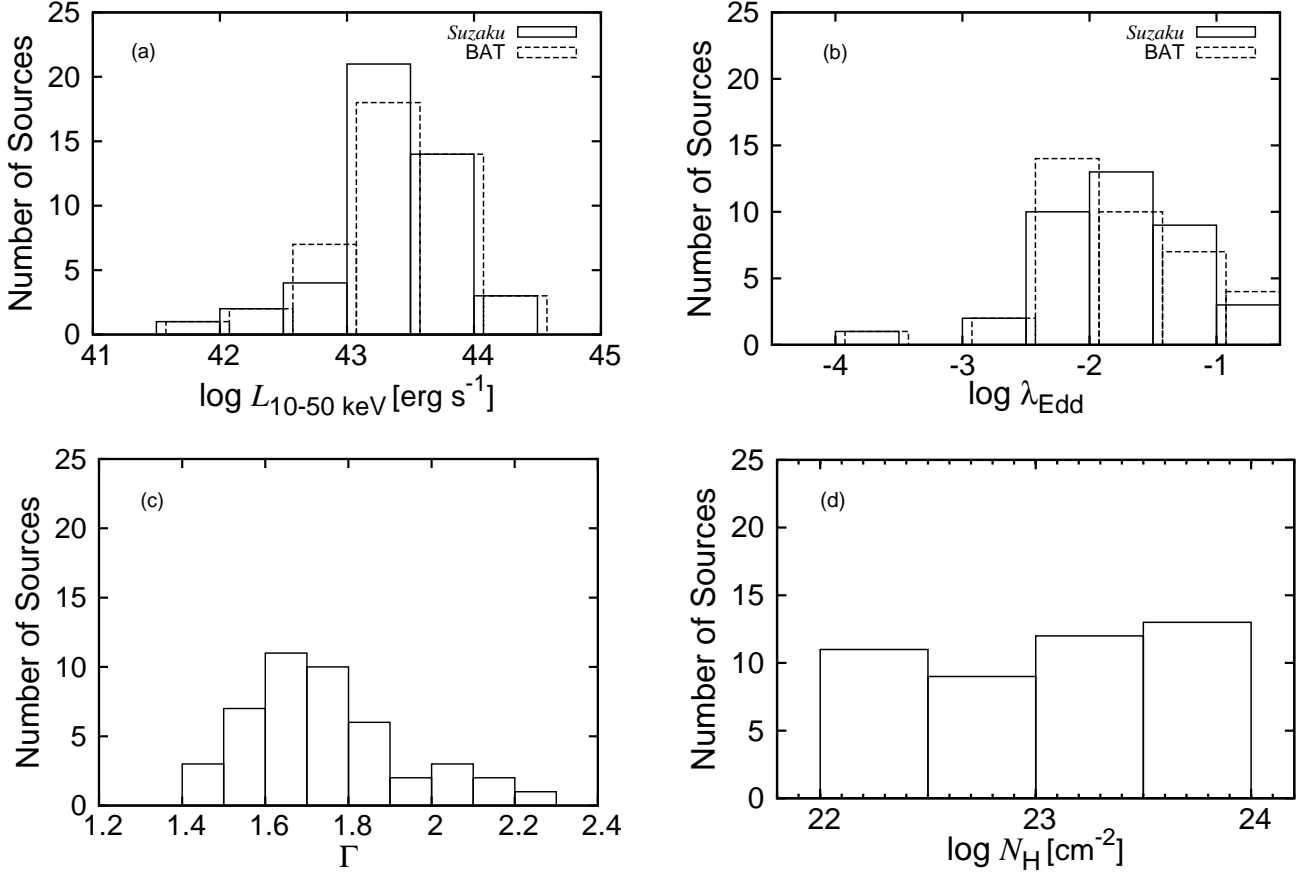


FIG. 2.— (a) distribution of absorption-corrected 10–50 keV luminosity. (b) distribution of Eddington ratio. (c) distribution of photon index. (d) distribution of hydrogen column density. The solid and dashed histograms in the upper figures refer to the luminosities measured with *Suzaku* and *Swift/BAT*, respectively. For clarity, the dashed histograms are slightly shifted to the right.

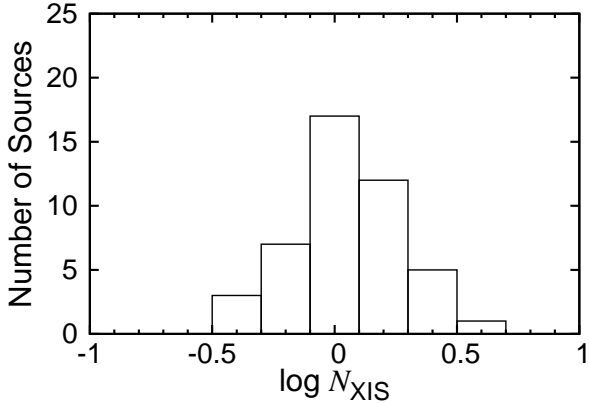


FIG. 3.— Distribution of the time variation constant of the cutoff power-law component between the *Suzaku* and *Swift/BAT* observations.

results for different combinations of parameters. If the correlation is found to be significant at >95% confidence level, then its best-fit regression line is plotted in the corresponding figure.

We examine possible time variability of N_{H} by compiling previous results in the literature obtained with *XMM-Newton*, *Chandra*, or *NuSTAR*. Also, if an object

was observed with *Suzaku* on multiple occasions, we analyze all available data with the same spectral model and derive N_{H} for each epoch. These results are summarized in Table E. Although we have to bear in mind that the best-fit N_{H} depends on the continuum model adopted, 4 objects (Mrk 1210, Mrk 348, NGC 1052, and NGC 4507) seem to show significant time variability of N_{H} by a factor of > 2 within 15 years. Nevertheless, we confirm that even if we adopt the averaged value of N_{H} instead of the *Suzaku* only result, it does not affect the sample selection ($22 \leq \log N_{\text{H}} < 24$) and our results on the correlations of N_{H} with other X-ray properties (Sections 4.1 and 4.2) and on the stacked X-ray spectral analysis (Section 4.3).

4.1. Basic X-ray Properties

Figure 2 shows distributions of the absorption-corrected 10–50 keV luminosity ($L_{10–50 \text{ keV}}$), Eddington ratio (λ_{Edd}), photon index (Γ), and hydrogen column density (N_{H}) of the whole sample. The mean and standard deviation are summarized in Table 3. In Figure 3, we plot the distribution of the time-variation constant, N_{xis} , which represents the luminosity change of the primary cutoff power-law component between the *Suzaku* and *Swift/BAT* observations. The mean and standard deviation are 0.05 ± 0.03 and 0.21 ± 0.04 . This suggests that a typical level of variability of the primary X-ray emission on timescales of \sim a day to several years is ~ 0.2

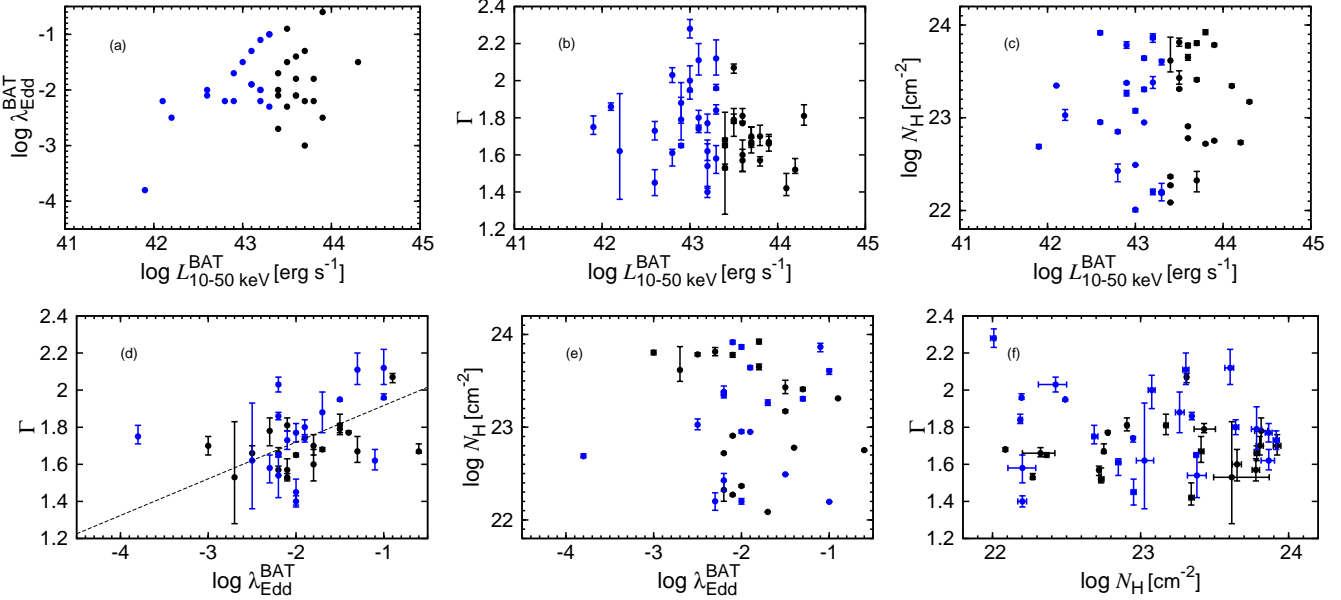


FIG. 4.— (a) correlation of Eddington ratio with 10–50 keV luminosity and regression function (dashed line). (b) correlation of photon index with 10–50 keV luminosity of $\Gamma = 8.6 - 0.16 \log L_{\text{10-50 keV}}^{\text{BAT}}$. (c) correlation of absorption column density with 10–50 keV luminosity. (d) correlation of photon index with Eddington ratio and regression function (dashed line) of $\Gamma = 2.11 + 0.20 \log \lambda_{\text{Edd}}^{\text{BAT}}$. (e) correlation of absorption column density with Eddington ratio. (f) correlation of photon index with absorption column density. The blue and black circles represent the MLAGNs ($L_{\text{10-50 keV}}^{\text{BAT}} \leq 43.3$) and HLAGNs ($L_{\text{10-50 keV}}^{\text{BAT}} > 43.3$), respectively.

TABLE 3
MEAN AND STANDARD DEVIATION OF SPECTRAL PARAMETERS

X	$r(X)$	$\sigma(X)$
(1)	(2)	(3)
$\log L_{\text{10-50 keV}}^{\text{Suzaku}}$	43.3 ± 0.08	0.53 ± 0.11
$\log L_{\text{10-50 keV}}^{\text{BAT}}$	43.3 ± 0.08	0.51 ± 0.11
$\log \lambda_{\text{Edd}}^{\text{Suzaku}}$	-1.9 ± 0.1	0.6 ± 0.1
$\log \lambda_{\text{Edd}}^{\text{BAT}}$	-1.9 ± 0.1	0.6 ± 0.1
Γ	1.74 ± 0.03	0.19 ± 0.04
$\log N_{\text{H}}$	23.1 ± 0.09	0.59 ± 0.12
$\log N_{\text{XIS}}$	0.05 ± 0.03	0.21 ± 0.04

NOTE. — Columns: (1) Parameter. (2) Mean of X. (3) Standard deviation of X.

dex.

Figure 4 shows correlations among $\log L_{\text{10-50 keV}}^{\text{BAT}}$, $\log \lambda_{\text{Edd}}^{\text{BAT}}$, Γ , and $\log N_{\text{H}}$. For easy check of any luminosity dependence, we divide our sample into two groups, moderate luminosity AGNs (MLAGNs) with $\log L_{\text{10-50 keV}}^{\text{BAT}} \leq 43.3$ and high luminosity ones (HLAGNs) with $\log L_{\text{10-50 keV}}^{\text{BAT}} > 43.3$, which consists of 24 and 21 objects, respectively. The criterion of $\log L_{\text{10-50 keV}}^{\text{BAT}}$ is determined so that the source numbers of the two subsamples become the same when we make spectral stacking analysis (Section 4.3).

As inferred from Figure 4(a), there is no significant $\log \lambda_{\text{Edd}}^{\text{BAT}} - \log L_{\text{10-50 keV}}^{\text{BAT}}$ correlation. However, when adopting the luminosity-dependent correction factor of Marconi et al. (2004), we find a significant correlation

with $P(\log L_{\text{10-50 keV}}^{\text{BAT}}, \log \lambda_{\text{Edd}}) = 2.9 \times 10^{-2}$.

We find that photon index increases with Eddington ratio ($P(\log \lambda_{\text{Edd}}^{\text{BAT}}, \Gamma) = 9.7 \times 10^{-3}$), but does not significantly correlates with luminosity ($P(\log L_{\text{10-50 keV}}^{\text{BAT}}, \Gamma) = 8.6 \times 10^{-2}$). The dependence of photon index on black hole mass is found to be rather weak, with $P(\log M_{\text{BH}}, \Gamma) = 5.0 \times 10^{-2}$ and $\rho(\log M_{\text{BH}}, \Gamma) = -0.32$. The positive $\Gamma - \log \lambda_{\text{Edd}}$ correlation for luminous AGNs was also reported previously (e.g., Shemmer et al. 2008; Brightman et al. 2013; Yang et al. 2015b). The slope we obtain ($b = 0.20 \pm 0.01$) is flatter than those obtained in previous studies (≈ 0.3 ; e.g., Shemmer et al. 2008), however. It may be because our sample lacks high-Eddington ratio, high-luminosity AGNs ($\log L_{\text{X}} > 44$), which likely show much softer spectra. Most of them are identified as type-1 AGNs, as expected from the luminosity dependence of the type-1 AGN fraction (e.g., Ueda et al. 2003, 2014; Hasinger 2008; Beckmann et al. 2009; Brightman & Nandra 2011; Burlon et al. 2011; Ricci et al. 2013). We also confirm that even if we adopt the bolometric correction factor of Marconi et al. (2004), the positive correlation remains tight with $P(\log \lambda_{\text{Edd}}^{\text{BAT}}, \Gamma) = 2.1 \times 10^{-2}$. Hence, the Eddington ratio may be an important parameter that determines the nature of the X-ray emitting corona (optical depth end electron temperature). Theoretically, this correlation can be explained if Compton cooling of the corona by seed photons becomes more efficient with increasing accretion rate, leading to a smaller Compton y-parameter, and hence a softer spectrum.

The hydrogen column density correlates with neither $\log L_{\text{10-50 keV}}^{\text{BAT}}$ nor $\log \lambda_{\text{Edd}}^{\text{BAT}}$. Also, there is no significant correlation between $\log N_{\text{H}}$ and Γ , supporting that the underlying continuum shape is properly determined without strong coupling with the absorption unlike the

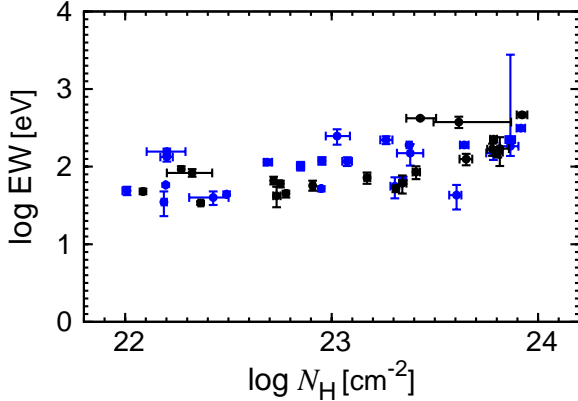


FIG. 5.— Correlation between the iron-K α EW and absorption column density. The blue and black circles represent the MLAGNs ($L_{10-50 \text{ keV}}^{\text{BAT}} \leq 43.3$) and HLAGNs ($L_{10-50 \text{ keV}}^{\text{BAT}} > 43.3$), respectively.

case of narrow band spectral analysis with limited photon statistics.

4.2. Reflected Emission from Distant, Cold Matter

The narrow iron-K α fluorescence line at ≈ 6.4 keV is originated from distant, cold matter around the nucleus. We conventionally call it “torus”, although its shape and size are still largely unknown. We significantly detect the iron-K α line for all the objects of our sample. Except for 5 objects, the EW with respect to the reflection continuum is found to be in a range of 0.5–3 keV, which is consistent with a theoretical prediction from reflection by optically thick, cold matter within variations of inclination (EW ~ 1 –2 keV; Matt et al. 1991) and of iron abundance by a factor of 2 (Matt et al. 1997). In the rest of objects (NGC 4388, NGC 5252, LEDA 170194, Mrk 520, and Mrk 915), the EW is very large (> 3 keV) because the reflection continuum (i.e., R) is apparently very weak. We interpret that the tori in these objects are Compton-thin, thus producing a much weaker hump at ~ 30 keV and absorption iron-K edge features than what the `pexrav` model predicts. In fact, we confirm that a Monte-Carlo based torus model by Ikeda et al. (2009) can well reproduce the spectra of these objects including the continuum and iron-K α emission line, as done in Tazaki et al. (2013), Kawamuro et al. (2013), and Kawamuro et al. (2016). Systematic application of numerical torus models to all spectra of our sample is a subject of future works.

The relative intensity of the iron-K α line to the underlying continuum contains critical information on the covering fraction and column density of the torus. Figure 5 plots the observed EW with respect to the total continuum against N_{H} . A systematic increase in EW with N_{H} is seen in $\log N_{\text{H}} > 23$, confirming previous results (e.g., Fukazawa et al. 2011; Brightman & Nandra 2011). This can be explained by the attenuation of the transmitted component by absorption at the same energy, which makes the EW of the iron K α line larger. Thus, EW is not a good indicator to discuss the torus structure.

To correct for the absorption effect in the continuum flux, we adopt the $L_{\text{K}\alpha}/L_{10-50 \text{ keV}}$ ratio instead

of the EW as proposed by Ricci et al. (2014). Figure 6 shows the correlations of $\log L_{10-50 \text{ keV}}^{\text{BAT}}$ with $\log L_{\text{K}\alpha}$ and $\log(L_{\text{K}\alpha}/L_{10-50 \text{ keV}})$. We first calculate the OLS bisector regression line of the $\log L_{\text{K}\alpha}$ – $\log L_{10-50 \text{ keV}}^{\text{BAT}}$ correlation. The correlation is significant with $P(\log L_{10-50 \text{ keV}}, \log L_{\text{K}\alpha}) = 4.1 \times 10^{-16}$. The regression line we obtain gives a negative correlation between $\log(L_{\text{K}\alpha}/L_{10-50 \text{ keV}})$ and $\log L_{10-50 \text{ keV}}^{\text{BAT}}$, as shown in Figure 6(b). The slope (-0.06 ± 0.04) is consistent with -0.11 ± 0.01 derived by Ricci et al. (2014).

Strength of the reflection component from the torus, R ($= \Omega/2\pi$), can be also used as an indicator of the torus covering fraction. Figure 7 shows correlations of R with $\log L_{10-50 \text{ keV}}^{\text{BAT}}$, $\log(L_{\text{K}\alpha}/L_{10-50 \text{ keV}})$, and $\log N_{\text{H}}$. We overplot the mean values of R with 1σ errors calculated in each region of the X-axis parameter from all objects (black) and from only objects whose R values are significantly measured (pink) (i.e., the lower and upper limits of R are larger than 0 and smaller than 2, respectively), by adopting the best-fit value listed in Table A. Most of the results are consistent within the errors between the two calculations and show the same trends against the X-axis parameter. Although the negative correlation of R with luminosity is not strong ($P(\log L_{10-50 \text{ keV}}, R) = 5.6 \times 10^{-2}$), this trend is confirmed in Section 4.3 by analyzing the stacked hard X-ray spectra of MLAGNs ($L_{10-50 \text{ keV}}^{\text{BAT}} \leq 43.3$) and HLAGNs ($L_{10-50 \text{ keV}}^{\text{BAT}} > 43.3$). On the other hand, the correlation between R and $\log(L_{\text{K}\alpha}/L_{10-50 \text{ keV}})$ is found to be significant with $P(\log(L_{\text{K}\alpha}/L_{10-50 \text{ keV}}), R) = 1.0 \times 10^{-2}$ and $\rho(\log(L_{\text{K}\alpha}/L_{10-50 \text{ keV}}), R) = 0.38$. This result supports that the reflection continuum and narrow iron-K α emission line originate from the same material (i.e., torus). We also find the trend that R is larger in more obscured AGNs, although the significance is not high in this plot (but see Section 4.3 for an analysis of averaged hard X-ray spectra of the moderately obscured AGNs with $\log N_{\text{H}} \leq 23$ and highly obscured ones with $\log N_{\text{H}} > 23$; hereafter MOAGNs and HOAGNs, respectively). This is expected if the direction-averaged column density and/or covering fraction of the torus is larger in AGNs with larger line-of-sight absorptions.

4.3. Average Hard X-ray Spectra

To investigate the average reflection strength in an alternative way, we analyze the *Swift*/BAT and HXD/PIN stacked hard X-ray spectra for the subsamples of MLAGNs and HLAGNs or those of MOAGNs and HOAGNs. Because only continuum emission is present above 14 keV, we do not make any K-correction in the summation, for simplicity, by excluding 3 distant AGNs at $z > 0.05$. A cutoff power-law plus its reflected component (`zpowerlw*zhighcet+pexrav` in the XSPEC terminology) is used to reproduce the continuum. The redshift is fixed to the mean value of each subsample. Even at energies above 14 keV, large absorption with $\log N_{\text{H}} \gtrsim 23.5$ is not negligible. To take into account this effect, we multiply the partial covering model, `zpcfabs`, to the above continuum. The covering fraction is set to the fraction of the integrated fluxes of AGNs with $\log N_{\text{H}} > 23.5$ in each subsample and the column density is fixed at their average value. Thus, the reflection strength, photon index,

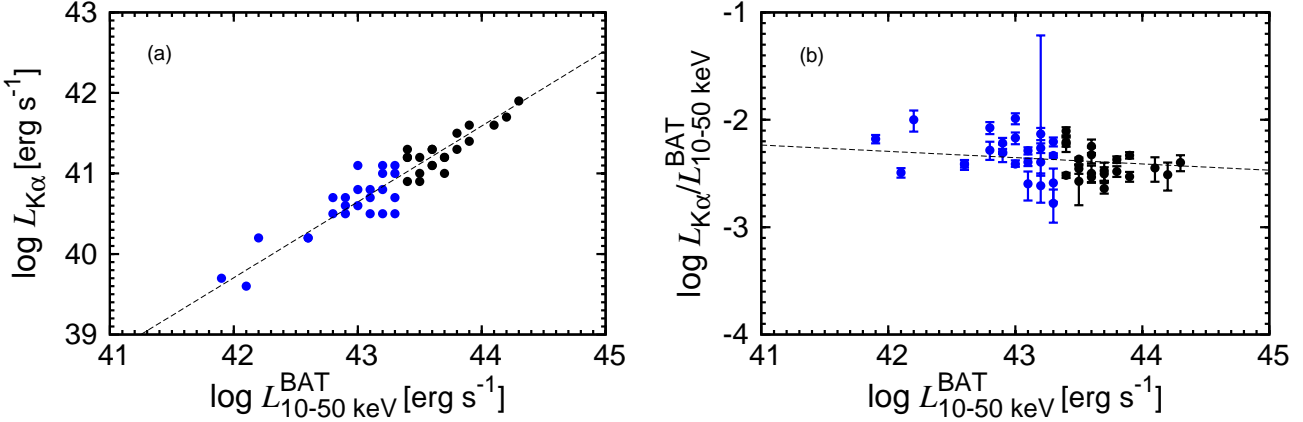


FIG. 6.— (a) correlation of iron-K α line luminosity with 10–50 keV luminosity and regression function (dashed line) of $\log L_{\text{K}\alpha} = 0.2 + 0.94 \log L_{10-50 \text{ keV}}$. (b) correlation of the iron-K α to 10–50 keV luminosity ratio with 10–50 keV luminosity and regression function (dashed line) of $\log(L_{\text{K}\alpha}/L_{10-50 \text{ keV}}) = 0.2 - 0.06 \log L_{10-50 \text{ keV}}$. The blue and black circles represent the MLAGNs ($L_{10-50 \text{ keV}}^{\text{BAT}} \leq 43.3$) and HLAGNs ($L_{10-50 \text{ keV}}^{\text{BAT}} > 43.3$), respectively. The dashed lines represent the regression line.

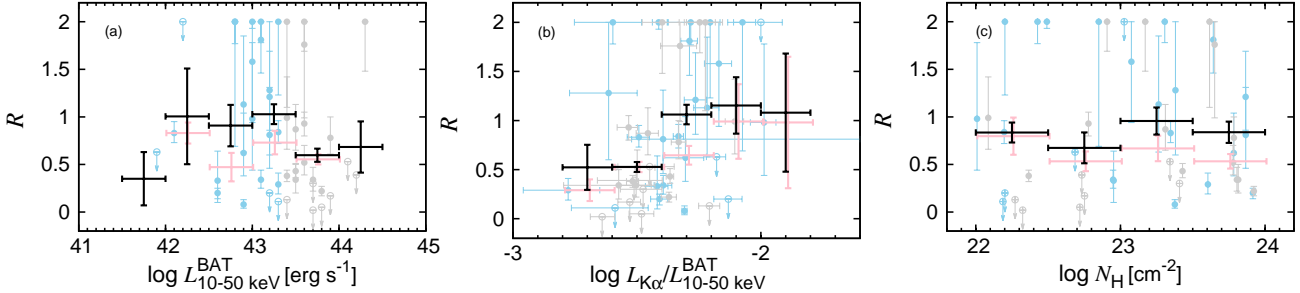


FIG. 7.— (a) correlation of reflection strength with 10–50 keV luminosity. (b) correlation of reflection strength with the iron-K α to 10–50 keV luminosity ratio. (c) correlation of reflection strength with absorption column density. The cyan and gray circles represent the MLAGNs ($L_{10-50 \text{ kev}}^{\text{BAT}} \leq 43.3$) and HLAGNs ($L_{10-50 \text{ kev}}^{\text{BAT}} > 43.3$), respectively. The open circles represent data with upper limits. The black lines represent the mean and 1σ error of R in each region for all objects, while the pink lines (slightly shifted to the right for clarity) for only objects whose R values are significantly measured.

and normalization are left as free parameters.

Figure 8 shows the unfolded spectra of *Swift*/BAT and HXD/PIN for the MLAGN ($L_{10-50 \text{ keV}}^{\text{BAT}} \leq 43.3$) and HLAGN ($L_{10-50 \text{ keV}}^{\text{BAT}} > 43.3$) subsamples, which contain the same number of sources (21), together with their best-fit models. Here, when fitting the HXD/PIN spectra, we fix the photon index at the best-fitting value obtained from each *Swift*/BAT spectrum. The MLAGN spectrum shows significantly stronger reflection strength ($R = 1.04^{+0.17}_{-0.19}$) than that of the HLAGNs ($R = 0.46^{+0.08}_{-0.09}$), consistent with the results suggested in Section 4.2. The confidence contours between photon index and R obtained from the *Swift*/BAT and HXD/PIN spectra are plotted in Figure 8(c) and (f). As noticed, the two results are compatible with each other, although the constraints obtained with the HXD/PIN data are much weaker owing to the limited energy band. Our findings support the luminosity-dependent unified AGN scheme.

We also make the same analysis to the subsamples of MOAGNs ($\log N_{\text{H}} \leq 23$) and HOAGNs ($\log N_{\text{H}} > 23$). The unfolded spectra with best-fit models and confidence contours between photon index and R are plotted in Figure 9. We find a significant difference in R between the

MOAGNs ($R = 0.59^{+0.09}_{-0.10}$) and HOAGNs ($R = 1.03^{+0.15}_{-0.17}$) from the *Swift*/BAT spectra, confirming the trend already reported in Section 4.2 more robustly. This is consistent with the previous work by Ricci et al. (2011), who carried out stacking *INTEGRAL* data. As we already mentioned, this implies that on average the covering fraction and/or average column density of a torus is larger in AGNs with larger line-of-sight absorptions.

In summary, the average reflection strength of the MLAGNs and HOAGNs is larger than that of the HLAGNs and MOAGNs, respectively.

4.4. Correlations among the X-ray and MIR properties

AGNs are also bright in the MIR band owing to emission of hot dust in the torus heated by the primary radiation from the central engine. In fact, a good correlation between the MIR and X-ray luminosities in AGNs has been reported by several works (Gandhi et al. 2009; Ichikawa et al. 2012; Matsuta et al. 2012; Asmus et al. 2015). Using our sample, we examine correlations of $\log L_{10-50 \text{ keV}}$ with $12 \mu\text{m}$ MIR luminosity $\log \lambda L_{12 \mu\text{m}}$ and $\log(\lambda L_{12 \mu\text{m}}/L_{10-50 \text{ keV}})$ as plotted in Figure 10. Here we refer to the nucleus $12 \mu\text{m}$ luminosities com-

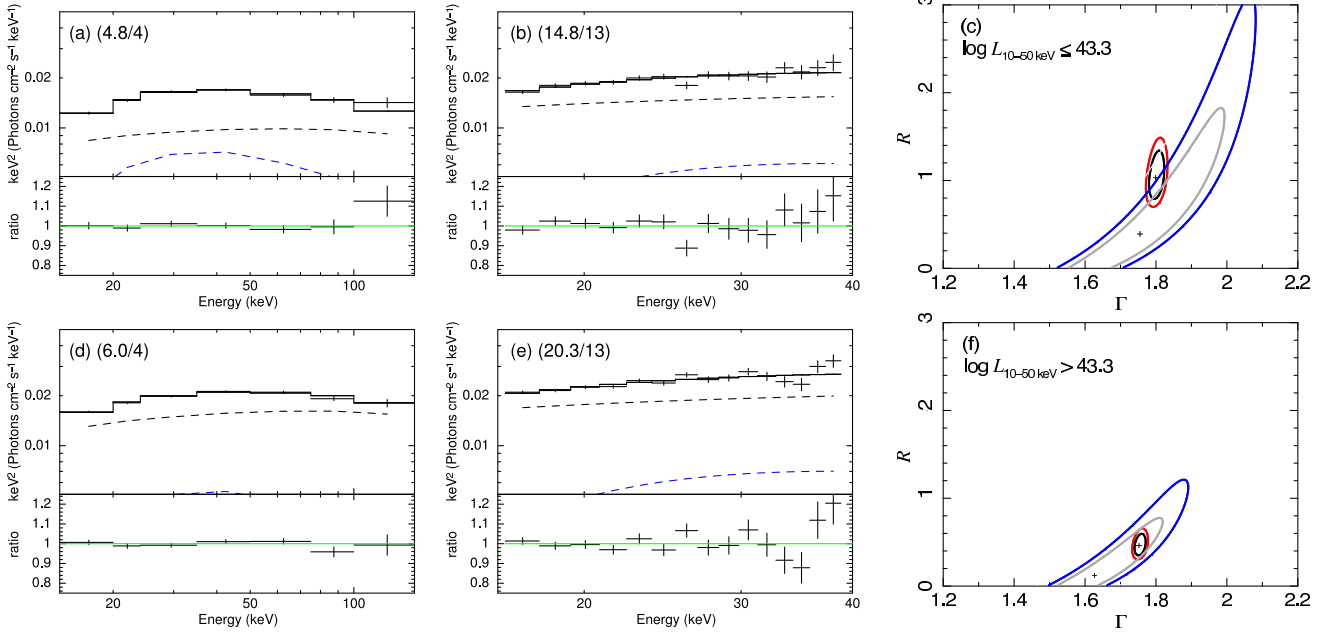


FIG. 8.— Upper: for the MLAGNs ($\log L_{\text{10-50 keV}}^{\text{BAT}} \leq 43.3$). Lower: for HLAGNs ($\log L_{\text{10-50 keV}}^{\text{BAT}} > 43.3$). (a), (d) the stacked *Swift/BAT* spectra. (b), (e) the stacked HXD/PIN spectra. (c), (f) confidence contours between photon index and reflection strength. In the left and central figures, the upper panel shows the spectrum with the best-fit model consisting of a cutoff power-law (black dashed line) and its reflection component (blue dashed line), whereas the lower panel plots the ratio of the data to the model. The reduced chi-squared statistic (χ^2/dof) for each fitting result is represented in the parenthesis. In the right figures, the constraint obtained from the *Swift/BAT* (HXD/PIN) spectrum is represented with the black (gray) and red (blue) lines, corresponding to $\Delta\chi^2 = 2.3$ and 4.6 , or the 68% and 90% confidence levels, respectively.

piled by Asmus et al. (2015) based on subarcsecond resolution imaging. For AGNs whose luminosities are not available in Asmus et al. (2015), we calculate those using the photometric data of Wide-field Infrared Survey Explorer (*WISE*; Wright et al. 2010). Because the spatial resolution of *WISE* is limited ($\sim 6''.5$ in the $12\ \mu\text{m}$ band), contamination from the host galaxy may not be ignorable in these data. Table 4 summarizes the compiled $\lambda L_{12\ \mu\text{m}}$ luminosities.

We obtain a tight $\log \lambda L_{12\ \mu\text{m}} - \log L_{\text{10-50 keV}}^{\text{BAT}}$ correlation with a slope $b = 0.92 \pm 0.07$ (0.91 ± 0.10) from the whole sample (that only with the high resolution MIR data). The slope is consistent with previous results (Ichikawa et al. 2012; Asmus et al. 2015). We confirm that the flux-flux correlation is also significant, indicating that the luminosity-luminosity correlation is robust against the Malmquist bias. The regression line yields a negative slope ($b = -0.08 \pm 0.07$) in the correlation between the MIR to 10–50 keV luminosity ratio ($\lambda L_{12\ \mu\text{m}}/L_{\text{10-50 keV}}^{\text{BAT}}$) and the 10–50 keV luminosity. As investigated in detail by Stalevski et al. (2016), $\lambda L_{12\ \mu\text{m}}/L_{\text{10-50 keV}}^{\text{BAT}}$ is predicted to monotonically increase with increasing covering factor, or decreasing half opening-angle, of the torus in the edge-on view (i.e., type-2 AGN) case. Here, the half opening-angle is defined as that between the polar axis and the upper edge of the torus. It is because the solid angle of the torus illuminated by the accretion disk increases with decreasing half opening-angle and consequently the reprocessed emission in the infrared band becomes stronger. Hence, the negative correlation of the MIR to X-ray luminosity ratio

with X-ray luminosity is consistent with the luminosity-dependent AGN unified model (e.g., Ueda et al. 2003; Maiolino et al. 2007; Lusso et al. 2013; Ricci et al. 2013).

4.5. X-ray and [O IV] Luminosity as AGN Power Indicator

Gas around the torus is excited by irradiation from the central engine and scatters a part of incident photons. Hence, it provides us with the information of the intrinsic luminosity even in obscured AGNs. To estimate the intrinsic AGN power, some authors proposed the usage of the [O IV] line (e.g., Meléndez et al. 2008; Rigby et al. 2009). This is because, compared with optical emission lines, [O IV] is much less affected by dust extinction in the interstellar matter and is less contaminated by starlight from the host galaxy due to the high ionization potential (54.9 eV). To investigate the correlation of the [O IV] line to 10–50 keV luminosity, another proxy of AGN luminosity, we compile the [O IV] luminosities ($L_{[\text{O IV}]}$) from the literature (Weaver et al. 2010; Weedman et al. 2012; Inami et al. 2013; Liu et al. 2014), as listed in Table 4. Figure 11(a) plots $\log L_{[\text{O IV}]}$ against $\log L_{\text{10-50 keV}}^{\text{BAT}}$. The correlation is insignificant with $P(\log L_{\text{10-50 keV}}^{\text{BAT}}, \log L_{[\text{O IV}]}) = 5.8 \times 10^{-1}$.

Previous studies reported that the $L_{[\text{O IV}]}/L_{\text{X}}$ ratio of type-2 AGNs may be higher than that of type-1 AGNs (e.g., Meléndez et al. 2008; Rigby et al. 2009; Liu et al. 2014). They suggested that the difference is ascribed to an underestimation of the X-ray luminosity due to obscuration in type-2 AGNs or to anisotropy of the intrinsic X-ray emission. For comparison, we overplot the

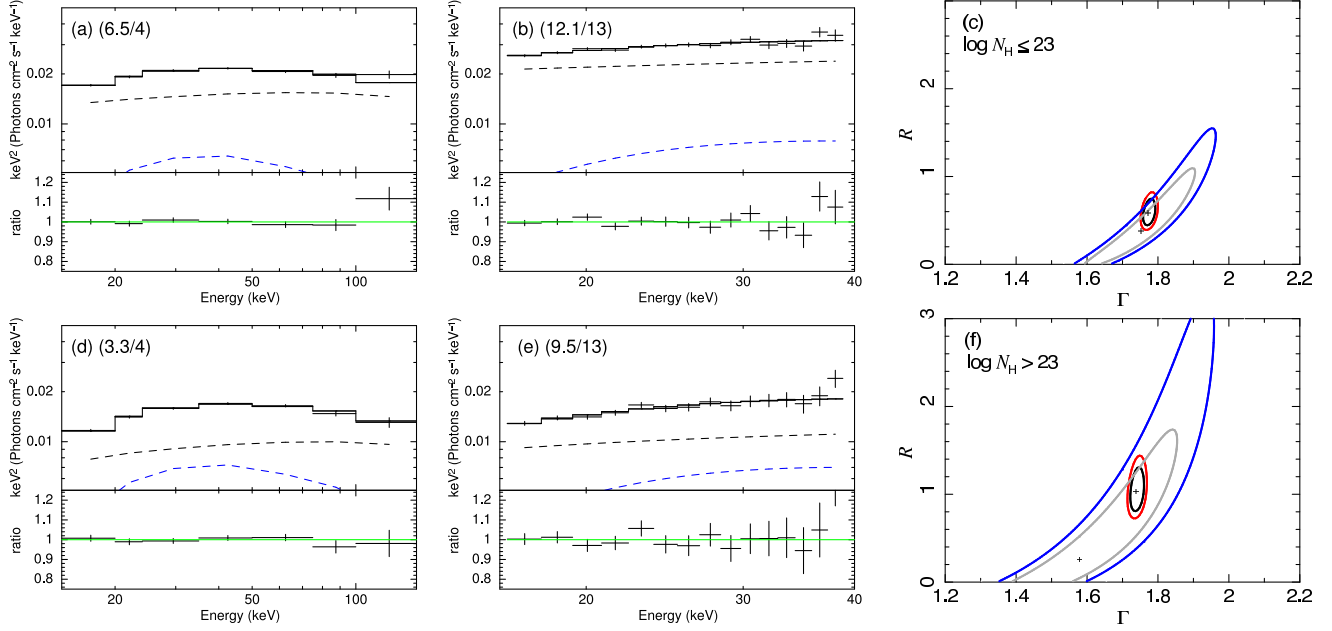


FIG. 9.— Same as Figure 8 but for the MOAGNs ($\log N_{\mathrm{H}} \leq 23$) in the upper figures and for the HOAGNs ($\log N_{\mathrm{H}} > 23$) in the lower figures.

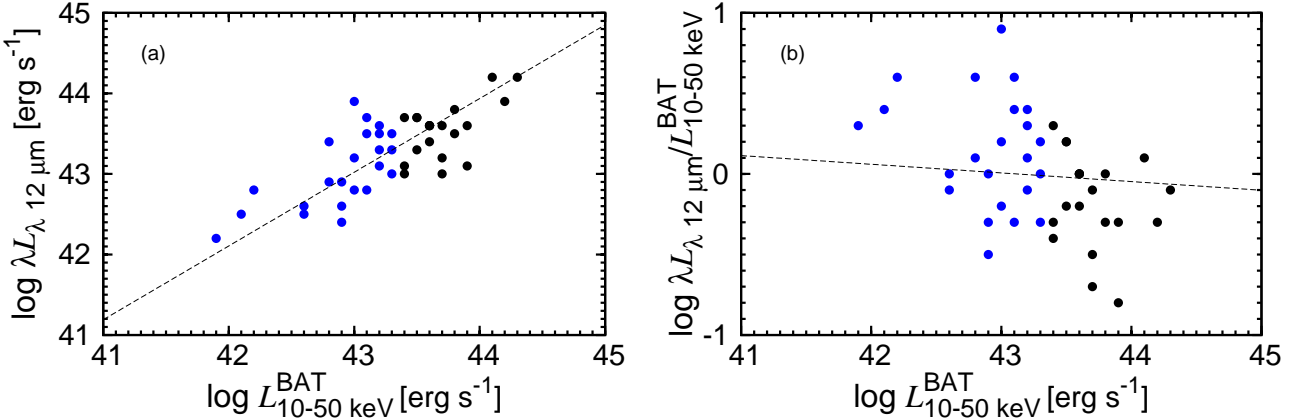


FIG. 10.— (a) correlation between 12 μm and 10–50 keV luminosities and regression function (dashed line) of $\log \lambda L_{12 \mu\text{m}} = 3.7 + 0.92 \log L_{10-50 \text{ keV}}^{\text{BAT}}$. (b) correlation between the 12 μm to 10–50 keV luminosity ratio and 10–50 keV luminosity and regression function (dashed line) of $\log(\lambda L_{12 \mu\text{m}}/L_{10-50 \text{ keV}}^{\text{BAT}}) = 3.7 - 0.08 \log L_{10-50 \text{ keV}}^{\text{BAT}}$. The blue and black circles represent the MLAGNs ($L_{10-50 \text{ keV}}^{\text{BAT}} \leq 43.3$) and HLAGNs ($L_{10-50 \text{ keV}}^{\text{BAT}} > 43.3$), respectively. The dashed lines represent the regression line.

relations of Liu et al. (2014) by converting the 14–195 keV luminosity into the 10–50 keV one with a power-law photon index of 1.7. As shown in Figure 11(a), the $L_{[\text{O IV}]}/L_X$ ratio of our sample is more similar to that of type-1 AGNs than that of the type-2 AGNs in Liu et al. (2014). As a result, we do not see significant difference in the $L_{[\text{O IV}]}/L_X$ ratio between type-1 and Compton-thin type-2 AGNs. This suggests that the anisotropy of X-ray emission is unlikely.

A notable finding is that most of low scattering-fraction AGNs (with best-fit $f_{\text{scat}} < 0.5\%$) show systematically low values of $L_{[\text{O IV}]}/L_{10-50 \text{ keV}}^{\text{BAT}}$ ratio than the average. Indeed, we find a significant correlation between the $L_{[\text{O IV}]}/L_{10-50 \text{ keV}}^{\text{BAT}}$ ratio and the scattered fraction

(see Figure 11(b)). The regression line is calculated with the OLS bisector method by ignoring objects without significant detection of the scattered component. We exclude Mrk 915 because of its apparently very high scattering fraction ($\sim 40\%$), which is much higher than typical values in obscured AGNs ($\sim 3\%$; Bianchi & Guainazzi 2007) and should be attributed to leaky or ionized absorbers. These results well agree with that by Ueda et al. (2015) that low scattering-fraction AGNs show low $[\text{O III}]$ to hard X-ray luminosity ratios on average. This supports the picture that a significant fraction of this population of AGNs are deeply “buried” in small opening-angle tori. This also implies that the $[\text{O IV}]$ luminosity may not be an ideal indicator of the intrinsic AGN power

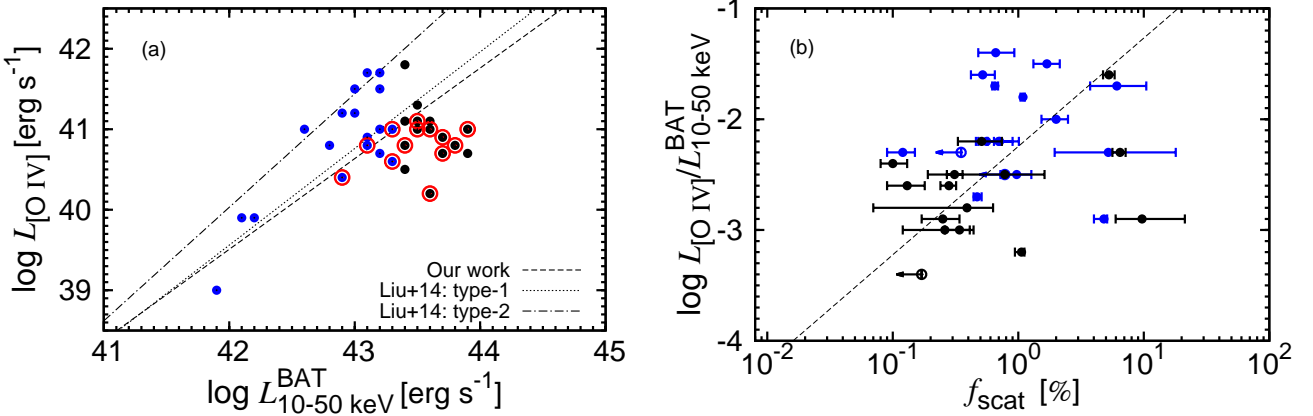


FIG. 11.— (a) correlation between [O IV] and 10–50 keV luminosities and regression function (dashed line) of $\log L_{\text{[O IV]}} = -7.8 + 1.13 \log L_{\text{10-50 keV}}$. The dotted and dot-dashed lines represent the regression lines obtained from the type-1 and type-2 AGN samples of Liu et al. (2014), respectively. (b) correlation between the [O IV] to 10–50 keV luminosity ratio and scattered fraction and regression function (dashed line) of $\log(L_{\text{[O IV]}}/L_{\text{10-50 keV}}^{\text{BAT}}) = -2.25 + 0.98 \log f_{\text{scat}}$. The blue, black, and red circles (only in the left figure) represent the MLAGNs ($L_{\text{10-50 keV}}^{\text{BAT}} \leq 43.3$), HLAGNs ($L_{\text{10-50 keV}}^{\text{BAT}} > 43.3$), and low scattering-fraction AGNs ($f_{\text{scat}} < 0.5\%$), respectively.

for the whole AGN population.

5. CONCLUSION

We have analyzed the broadband (0.5–150 keV) X-ray spectra of 45 local, moderately obscured (Compton-thin) AGNs observed with *Suzaku* and *Swift/BAT* in a uniform manner. The broadband X-ray spectra are basically well reproduced with the baseline model composed of an absorbed cutoff power-law component, a scattered component, and a (unabsorbed/absorbed) reflection component with a fluorescent iron-K α line. Additional components such as emission/absorption lines and optically-thin thermal emission in the host galaxy are also taken into account if required. The main conclusions of our work are summarized as follows.

1. We evaluate time variation of the luminosity of the primary power-law component between the *Suzaku* and 70-month averaged *Swift/BAT* observations. The standard deviation is ~ 0.2 dex, which can be regarded as typical variability on timescales of \sim a day to several years.
2. We find a significant correlation of photon index with Eddington ratio, but not with luminosity or black hole mass. This is consistent with previous results (Shemmer et al. 2008; Brightman et al. 2013; Yang et al. 2015b).
3. A narrow iron-K α line is significantly detected in all objects. The $L_{\text{K}\alpha}/L_{\text{10-50 keV}}$ ratio decreases with luminosity, supporting the luminosity-dependent AGN unified model where the covering fraction of tori decreases with luminosity.
4. The average reflection strength derived from stacked spectra above 14 keV is found to be larger in less luminous ($\log L_{\text{10-50 keV}} \leq 43.3$) or heavily obscured ($\log N_{\text{H}} > 23$) AGNs than in more luminous ($\log L_{\text{10-50 keV}} > 43.3$) or lightly obscured AGNs ($\log N_{\text{H}} \leq 23$), respectively.

5. We confirm strong correlation between the X-ray and MIR luminosities ($\log \lambda L_{\lambda 12 \mu\text{m}} - \log L_{\text{10-50 keV}}$), which results in a negative $\log(\lambda L_{\lambda 12 \mu\text{m}}/L_{\text{10-50 keV}}) - \log L_{\text{10-50 keV}}$ correlation. This is again consistent with the luminosity-dependent unified model.
6. The average [O IV] line to hard X-ray luminosity ratio obtained from our sample is lower than previous estimates using other samples of type-2 AGNs. In particular, this ratio is found to be significantly lower in low scattering-fraction AGNs. This suggests that the [O IV] luminosity may significantly underestimate the intrinsic luminosity of AGNs deeply buried in small opening-angle tori.

TABLE 4
MIR LUMINOSITY

Target Name (1)	$\log L_{12\mu\text{m}}$ (2)	Ref. (3)	$\log L_{12\mu\text{m}}$ (3)	$\log L_{[\text{O IV}]}$ (4)	Ref. (5)	$\log L_{[\text{O IV}]}$ (5)
2MASX J0216+5126
2MASX J0248+2630	44.17 ± 0.01	W	
2MASX J0318+6829	43.90 ± 0.01	W	
2MASX J0350-5018	43.04 ± 0.01	W		40.5	1	
2MASX J0444+2813	42.58 ± 0.01	W	
2MASX J0505-2351	43.57 ± 0.13	A		40.7	1	
2MASX J0911+4528	43.03 ± 0.01	W		41.0	1	
2MASX J1200+0648	43.56 ± 0.01	W	
Ark 347	43.27 ± 0.11	A		41.5	1	
ESO 103-035	43.68 ± 0.19	A		41.1	2	
ESO 263-G013	43.56 ± 0.03	A	
ESO 297-G018	43.03 ± 0.07	A		40.7	1	
ESO 506-G027	43.80 ± 0.04	A		40.8	1	
Fairall 49	43.93 ± 0.20	A		41.5	2	
Fairall 51	43.39 ± 0.04	A		40.8	2	
IC 4518A	43.47 ± 0.06	A		41.7	3	
LEDA 170194	43.52 ± 0.08	A	
MCG +04-48-002	43.59 ± 0.01	W		40.7	4	
MCG -01-05-047	42.88 ± 0.15	A	
MCG -02-08-014	42.84 ± 0.07	A	
MCG -05-23-016	43.45 ± 0.04	A		40.6	2	
Mrk 1210	43.67 ± 0.01	W		40.9	1	
Mrk 1498	44.24 ± 0.01	W	
Mrk 18	42.84 ± 0.01	W		39.9	2	
Mrk 348	43.59 ± 0.01	W		41.0	2	
Mrk 417	43.58 ± 0.01	W		41.1	1	
Mrk 520		41.8	1	
Mrk 915	43.45 ± 0.04	A		41.7	1	
NGC 1052	42.20 ± 0.06	A		39.0	2	
NGC 1142	43.08 ± 0.20	A		41.0	3	
NGC 2110	43.08 ± 0.06	A		40.8	2	
NGC 235A	43.30 ± 0.16	A		41.3	4	
NGC 3081	42.49 ± 0.07	A		41.0	2	
NGC 3431	42.91 ± 0.01	W	
NGC 4388	42.38 ± 0.07	A		41.2	2	
NGC 4507	43.68 ± 0.04	A		41.0	2	
NGC 4992	43.44 ± 0.09	A		40.2	1	
NGC 5252	43.16 ± 0.04	A		40.9	1	
NGC 526A	43.68 ± 0.05	A		41.1	2	
NGC 5506	43.16 ± 0.03	A		41.2	2	
NGC 6300	42.51 ± 0.11	A		39.9	3	
NGC 7172	42.81 ± 0.04	A		40.8	2	
NGC 788	43.15 ± 0.05	A		41.0	2	
UGC 03142	43.25 ± 0.01	W	
UGC 12741	42.63 ± 0.01	W		40.4	2	

NOTE. — (1) Galaxy name. (2) 12 μm luminosity. (3) References for the 12 μm luminosity: (A) Asmus et al. (2015), (W) the data taken from the ALLWISE Source Catalog (Wright et al. 2010). (4) [O IV] luminosity. (5) References for the [O IV] luminosity: (1) Weedman et al. (2012) (2) Weaver et al. (2010) (3) Liu et al. (2014) (4) Inami et al. (2013).

Part of this work was financially supported by the Grant-in-Aid for JSPS Fellows for young researchers (T.K.) and for Scientific Research 26400228 (Y.U.). We acknowledge financial support from the CONICYT-Chile grants “EMBIGGEN” Anillo ACT1101 (CR), FONDECYT 1141218 (CR), and Basal-CATA PFB-06/2007

(CR). This research has made use of the NASA/ IPAC Infrared Science Archive, which is operated by the Jet Propulsion Laboratory, California Institute of Technology, under contract with the National Aeronautics and Space Administration.

REFERENCES

- Aird, J., Coil, A. L., Georgakakis, A., et al. 2015, MNRAS, 451, 1892
 Anders, E., & Grevesse, N. 1989, Geochim. Cosmochim. Acta, 53, 197
 Antonucci, R. 1993, ARA&A, 31, 473
 Asmus, D., Gandhi, P., Höning, S. F., Smette, A., & Duschl, W. J. 2015, MNRAS, 454, 766
 Awaki, H., Murakami, H., Ogawa, Y., & Leighly, K. M. 2006, ApJ, 645, 928
 Balestra, I., Bianchi, S., & Matt, G. 2004, A&A, 415, 437
 Baumgartner, W. H., Tueller, J., Markowitz, A. G., et al. 2013, ApJS, 207, 19
 Beckmann, V., Soldi, S., Ricci, C., et al. 2009, A&A, 505, 417
 Bennert, N., Jungwiert, B., Komossa, S., Haas, M., & Chini, R. 2006, A&A, 459, 55
 Beuchert, T., Markowitz, A. G., Krauß, F., et al. 2015, A&A, 584, A82
 Bianchi, S., & Guainazzi, M. 2007, in American Institute of Physics Conference Series, Vol. 924, The Multicolored Landscape of Compact Objects and Their Explosive Origins, ed. T. di Salvo, G. L. Israel, L. Piersant, L. Burderi, G. Matt, A. Tornambe, & M. T. Menna, 822–829
 Braito, V., Ballo, L., Reeves, J. N., et al. 2013, MNRAS, 428, 2516
 Brenneman, L. W., Weaver, K. A., Kadler, M., et al. 2009, ApJ, 698, 528
 Brightman, M., & Nandra, K. 2011, MNRAS, 413, 1206
 Brightman, M., Silverman, J. D., Mainieri, V., et al. 2013, MNRAS, 433, 2485
 Burlon, D., Ajello, M., Greiner, J., et al. 2011, ApJ, 728, 58
 Comastri, A., Iwasawa, K., Gilli, R., et al. 2010, ApJ, 717, 787
 Dadina, M. 2008, A&A, 485, 417
 Dadina, M., Guainazzi, M., Cappi, M., et al. 2010, A&A, 516, A9
 de Rosa, A., Panessa, F., Bassani, L., et al. 2012, MNRAS, 420, 2087
 Diamond-Stanic, A. M., Rieke, G. H., & Rigby, J. R. 2009, ApJ, 698, 623
 Diamond-Stanic, A. M., & Rieke, G. H. 2012, ApJ, 746, 168
 Dopita, M. A., Ho, L.-T., Dressel, L. L., et al. 2015, ApJ, 801, 42
 Dovčiak, M., Karas, V., & Yaqoob, T. 2004, ApJS, 153, 205
 Eguchi, S., Ueda, Y., Awaki, H., et al. 2011, ApJ, 729, 31
 Eguchi, S., Ueda, Y., Terashima, Y., Mushotzky, R., & Tueller, J. 2009, ApJ, 696, 1657
 Fukazawa, Y., Mizuno, T., Watanabe, S., et al. 2009, PASJ, 61, S17
 Fukazawa, Y., Hiragi, K., Mizuno, M., et al. 2011, ApJ, 727, 19
 Gandhi, P., Horst, H., Smette, A., et al. 2009, A&A, 502, 457
 Gandhi, P., Yamada, S., Ricci, C., et al. 2015, MNRAS, 449, 1845
 Gandhi, P., Terashima, Y., Yamada, S., et al. 2013, ApJ, 773, 51
 George, I. M., & Fabian, A. C. 1991, MNRAS, 249, 352
 Gofford, J., Reeves, J. N., Tombesi, F., et al. 2013, MNRAS, 430, 60
 Gruber, D. E., Matteson, J. L., Peterson, L. E., & Jung, G. V. 1999, ApJ, 520, 124
 Guainazzi, M. 2002, MNRAS, 329, L13
 Guainazzi, M., Fabian, A. C., Iwasawa, K., Matt, G., & Fiore, F. 2005, MNRAS, 356, 295
 Harrison, F. A., Craig, W. W., Christensen, F. E., et al. 2013, ApJ, 770, 103
 Hasinger, G. 2008, A&A, 490, 905
 Hernández-García, L., González-Martín, O., Masegosa, J., & Márquez, I. 2014, A&A, 569, A26
 Hernández-García, L., Masegosa, J., González-Martín, O., & Márquez, I. 2015, A&A, 579, A90
 Ichikawa, K., Ueda, Y., Terashima, Y., et al. 2012, ApJ, 754, 45
 Ikeda, S., Awaki, H., & Terashima, Y. 2009, ApJ, 692, 608
 Inami, H., Armus, L., Charmandaris, V., et al. 2013, ApJ, 777, 156
 Ishisaki, Y., Maeda, Y., Fujimoto, R., et al. 2007, PASJ, 59, 113
 Isobe, T., Feigelson, E. D., Akritas, M. G., & Babu, G. J. 1990, ApJ, 364, 104
 Iwasawa, K., Lee, J. C., Young, A. J., Reynolds, C. S., & Fabian, A. C. 2004, MNRAS, 347, 411
 Kalberla, P. M. W., Burton, W. B., Hartmann, D., et al. 2005, A&A, 440, 775
 Kawamuro, T., Ueda, Y., Tazaki, F., & Terashima, Y. 2013, ApJ, 770, 157
 Kawamuro, T., Ueda, Y., Tazaki, F., Terashima, Y., & Mushotzky, R. 2016, arXiv:1604.07915
 Keck, M. L., Brenneman, L. W., Ballantyne, D. R., et al. 2015, ApJ, 806, 149
 Khorunzhev, G. A., Sazonov, S. Y., Burenin, R. A., & Tkachenko, A. Y. 2012, Astronomy Letters, 38, 475
 Koyama, K., Tsunemi, H., Dotani, T., et al. 2007, PASJ, 59, 23
 LaMassa, S. M., Heckman, T. M., & Ptak, A. 2012, ApJ, 758, 82
 Lawrence, A. 1991, MNRAS, 252, 586
 Liu, T., Wang, J.-X., Yang, H., Zhu, F.-F., & Zhou, Y.-Y. 2014, ApJ, 783, 106
 Lobban, A. P., & Vaughan, S. 2014, MNRAS, 439, 1575
 Lusso, E., Hennawi, J. F., Comastri, A., et al. 2013, ApJ, 777, 86
 Magdziarz, P., & Zdziarski, A. A. 1995, MNRAS, 273, 837
 Maiolino, R., Shemmer, O., Imanishi, M., et al. 2007, A&A, 468, 979
 Malizia, A., Bassani, L., Bazzano, A., et al. 2012, MNRAS, 426, 1750
 Marchese, E., Braito, V., Reeves, J. N., et al. 2014, MNRAS, 437, 2806
 Marconi, A., Risaliti, G., Gilli, R., et al. 2004, MNRAS, 351, 169
 Marinucci, A., Risaliti, G., Wang, J., et al. 2013, MNRAS, 429, 2581
 Marinucci, A., Matt, G., Bianchi, S., et al. 2015, MNRAS, 447, 160
 Matsuta, K., Gandhi, P., Dotani, T., et al. 2012, ApJ, 753, 104
 Matt, G., Perola, G. C., & Piro, L. 1991, A&A, 247, 25
 Matt, G., Fabian, A. C., & Reynolds, C. S. 1997, MNRAS, 289, 175
 Matt, G. 2002, MNRAS, 337, 147
 Matt, G., Bianchi, S., Awaki, H., et al. 2009, A&A, 496, 653
 Meléndez, M., Kraemer, S. B., Armentrout, B. K., et al. 2008, ApJ, 682, 94
 Mitsuda, K., Bautz, M., Inoue, H., et al. 2007, PASJ, 59, 1
 Miyazawa, T., Haba, Y., & Kunieda, H. 2009, PASJ, 61, 1331
 Nandra, K., O’Neill, P. M., George, I. M., & Reeves, J. N. 2007, MNRAS, 382, 194
 Noda, H., Makishima, K., Yamada, S., et al. 2014, ApJ, 794, 2
 Noguchi, K., Terashima, Y., & Awaki, H. 2009, ApJ, 705, 454
 Panessa, F., Tarchi, A., Castangia, P., et al. 2015, MNRAS, 447, 1289
 Patrick, A. R., Reeves, J. N., Porquet, D., et al. 2012, MNRAS, 426, 2522
 Reeves, J. N., Awaki, H., Dewangan, G. C., et al. 2007, PASJ, 59, 301
 Ricci, C., Paltani, S., Awaki, H., et al. 2013, A&A, 553, A29
 Ricci, C., Ueda, Y., Koss, M. J., et al. 2015, ApJ, 815, L13
 Ricci, C., Ueda, Y., Paltani, S., et al. 2014, MNRAS, 441, 3622
 Ricci, C., Walter, R., Courvoisier, T. J.-L., & Paltani, S. 2011, A&A, 532, A102
 Rigby, J. R., Diamond-Stanic, A. M., & Aniano, G. 2009, ApJ, 700, 1878
 Risaliti, G., Elvis, M., & Nicastro, F. 2002, ApJ, 571, 234
 Risaliti, G., Elvis, M., Bianchi, S., & Matt, G. 2010, MNRAS, 406, L20
 Rivers, E., Markowitz, A., Rothschild, R., et al. 2014, ApJ, 786, 126
 Ross, R. R., & Fabian, A. C. 2005, MNRAS, 358, 211
 Sazonov, S., Churazov, E., Revnivtsev, M., Vikhlinin, A., & Sunyaev, R. 2005, A&A, 444, L37
 Shemmer, O., Brandt, W. N., Netzer, H., Maiolino, R., & Kaspi, S. 2008, ApJ, 682, 81
 Shirai, H., Fukazawa, Y., Sasada, M., et al. 2008, PASJ, 60, S263
 Shu, X. W., Yaqoob, T., & Wang, J. X. 2010, ApJS, 187, 581
 Stalevski, M., Ricci, C., Ueda, Y., et al. 2016, ArXiv e-prints, arXiv:1602.06954
 Svoboda, J., Beuchert, T., Guainazzi, M., et al. 2015, A&A, 578, A96
 Takahashi, T., Abe, K., Endo, M., et al. 2007, PASJ, 59, 35
 Tanaka, Y., Nandra, K., Fabian, A. C., et al. 1995, Nature, 375, 659
 Tanimoto, A., Ueda, Y., Kawamuro, T., & Ricci, C. 2016, ArXiv e-prints, arXiv:1601.05056

- Tazaki, F., Ueda, Y., Terashima, Y., & Mushotzky, R. F. 2011, ApJ, 738, 70
- Tazaki, F., Ueda, Y., Terashima, Y., Mushotzky, R. F., & Tombesi, F. 2013, ApJ, 772, 38
- Tombesi, F., Cappi, M., Reeves, J. N., et al. 2011, ApJ, 742, 44
- Tripathi, S., Misra, R., Dewangan, G. C., et al. 2013, ApJ, 773, 130
- Tripp, M. L., Reynolds, C. S., Koss, M., Mushotzky, R. F., & Winter, L. M. 2011, ApJ, 736, 81
- Ueda, Y., Akiyama, M., Hasinger, G., Miyaji, T., & Watson, M. G. 2014, ApJ, 786, 104
- Ueda, Y., Akiyama, M., Ohta, K., & Miyaji, T. 2003, ApJ, 598, 886
- Ueda, Y., Eguchi, S., Terashima, Y., et al. 2007, ApJ, 664, L79
- Ueda, Y., Hashimoto, Y., Ichikawa, K., et al. 2015, ApJ, 815, 1
- Vasudevan, R. V., & Fabian, A. C. 2009, MNRAS, 392, 1124
- Vasudevan, R. V., Fabian, A. C., Gandhi, P., Winter, L. M., & Mushotzky, R. F. 2010, MNRAS, 402, 1081
- Vasudevan, R. V., Fabian, A. C., Mushotzky, R. F., et al. 2013, MNRAS, 431, 3127
- Wang, J.-M., & Zhang, E.-P. 2007, ApJ, 660, 1072
- Weaver, K. A., Meléndez, M., Mushotzky, R. F., et al. 2010, ApJ, 716, 1151
- Weedman, D., Sargsyan, L., Lebouteiller, V., Houck, J., & Barry, D. 2012, ApJ, 761, 184
- Winter, L. M., Mushotzky, R. F., Tueller, J., & Markwardt, C. 2008, ApJ, 674, 686-710
- Winter, L. M., Mushotzky, R. F., Reynolds, C. S., & Tueller, J. 2009a, ApJ, 690, 1322
- Winter, L. M., Mushotzky, R. F., Terashima, Y., & Ueda, Y. 2009b, ApJ, 701, 1644
- Winter, L. M., Lewis, K. T., Koss, M., et al. 2010, ApJ, 710, 503
- Wright, E. L., Eisenhardt, P. R. M., Mainzer, A. K., et al. 2010, AJ, 140, 1868
- Yang, Q.-X., Xie, F.-G., Yuan, F., et al. 2015b, MNRAS, 447, 1692
- Zhang, S.-Y., Bian, W.-H., & Huang, K.-L. 2008, A&A, 488, 113

APPENDIX
BROADBAND X-RAY SPECTRA AND BEST-FITTING MODELS

TABLE A
 BEST-FIT PARAMETERS

Target Name (1)	$N_{\text{H}}^{\text{Gal}}$ (2)	A_{pl} (3)	N_{XIS} (4)	N_{H} (5)	$N_{\text{H}}^{\text{ref}}$ (6)	N_{H}^{pc} (7)	f_{pc} (8)	Γ (9)	f_{scat} (10)	R (11)	kT_1 (12)	kT_2 (13)	χ^2/dof (14)
2MASX J0216+5126	14.2	$2.96^{+0.40}_{-0.35}$	$0.90^{+0.11}_{-0.07}$	$1.54^{+0.05}_{-0.04}$	$1.84^{+0.03}_{-0.02}$	$0.64^{+0.37}_{-0.38}$	$0.00^{+0.11}_{-0.00}$	430.3/403
2MASX J0248+2630	10.3	$1.02^{+0.27}_{-0.22}$	$1.84^{+0.42}_{-0.16}$	$22.01^{+1.01}_{-0.74}$	$1.42^{+0.08}_{-0.04}$	$2.41^{+0.67}_{-0.53}$	$0.05^{+0.48}_{-0.05}$	96.0/115
2MASX J0318+6829	30.8	$0.88^{+0.10}_{-0.16}$	$1.45^{+0.33}_{-0.12}$	$5.41^{+0.25}_{-0.20}$	$1.52^{+0.06}_{-0.02}$	$3.63^{+0.92}_{-0.56}$	$0.00^{+0.39}_{-0.00}$	278.6/234
2MASX J0350-5018	1.16	$0.40^{+0.85}_{-0.23}$	$0.73^{+0.51}_{-0.37}$	41^{+33}_{-10}	$1.53^{+0.30}_{-0.25}$	$9.7^{+11.5}_{-3.7}$	$2.00^{+0.90}_{-0.90}$	31.4/41
2MASX J0444+2813	17.8	$1.47^{+0.31}_{-0.34}$	$0.86^{+0.09}_{-0.08}$	$8.97^{+0.35}_{-0.34}$	1.45 ± 0.07	$0.83^{+0.25}_{-0.22}$	$0.33^{+0.31}_{-0.23}$	239.1/230
2MASX J0505-2351	2.12	$4.47^{+0.29}_{-0.20}$	$0.89^{+0.04}_{-0.05}$	$5.65^{+0.10}_{-0.12}$...	$12.0^{+5.0}_{-3.9}$	0.29 ± 0.01	$1.67^{+0.04}_{-0.01}$	$1.06^{+0.06}_{-0.12}$	$0.12^{+0.03}_{-0.12}$	722.3/711
2MASX J0911+4528	1.23	$6.7^{+2.8}_{-2.0}$	$0.69^{+0.14}_{-0.10}$	$40.3^{+2.2}_{-3.2}$	$2.12^{+0.10}_{-0.09}$	$0.00^{+0.35}_{-0.00}$	$0.29^{+0.12}_{-0.10}$	110.2/96
2MASX J1200+0648	1.18	$1.44^{+0.32}_{-0.21}$	$2.78^{+0.34}_{-0.38}$	$8.09^{+0.21}_{-0.18}$	$1.81^{+0.04}_{-0.03}$	$0.19^{+0.33}_{-0.19}$	$2.00^{+0.31}_{-0.31}$	406.9/435
Ark 347	2.30	$0.73^{+0.50}_{-0.32}$	$0.50^{+0.17}_{-0.14}$	$24.0^{+3.8}_{-3.3}$	1.54 ± 0.12	$6.1^{+4.4}_{-2.4}$	$1.28^{+0.72}_{-0.68}$	$1.26^{+0.35}_{-0.20}$...	56.7/46
ESO 103-035	5.71	$28.6^{+3.4}_{-3.6}$	$1.27^{+0.07}_{-0.05}$	$20.45^{+0.37}_{-0.44}$	$4.6^{+1.3}_{-1.1}$	$55.9^{+8.8}_{-9.5}$	$0.33^{+0.03}_{-0.04}$	$2.07^{+0.02}_{-0.03}$	$0.10^{+0.03}_{-0.02}$	$0.87^{+0.26}_{-0.22}$	$1.07^{+0.27}_{-0.15}$...	1126.1/1096
ESO 263-G013	10.2	$2.80^{+0.79}_{-0.61}$	$0.94^{+0.13}_{-0.11}$	$25.64^{+1.17}_{-0.96}$	$1.67^{+0.08}_{-0.06}$	$0.71^{+0.24}_{-0.25}$	$0.05^{+0.25}_{-0.05}$	$0.93^{+0.13}_{-0.17}$...	96.7/108
ESO 297-G018	1.63	$5.23^{+1.13}_{-0.95}$	$0.96^{+0.10}_{-0.08}$	$63.8^{+3.6}_{-3.4}$	1.70 ± 0.05	$0.26^{+0.15}_{-0.14}$	$0.34^{+0.13}_{-0.12}$	42.9/48
ESO 506-G027	5.45	$7.4^{+1.7}_{-1.4}$	$0.54^{+0.05}_{-0.04}$	$83.7^{+5.1}_{-4.8}$	$1.70^{+0.06}_{-0.05}$	$0.34^{+0.10}_{-0.08}$	0.22 ± 0.05	70.0/60
Fairall 49	6.47	$8.5^{+2.1}_{-2.4}$	$2.06^{+0.88}_{-0.43}$	$1.02^{+0.03}_{-0.05}$...	$3.20^{+0.85}_{-0.95}$	$0.22^{+0.03}_{-0.04}$	2.28 ± 0.05	$1.69^{+0.45}_{-0.37}$	$0.98^{+0.80}_{-0.54}$	1949.8/1753
Fairall 51	6.97	$5.98^{+1.12}_{-0.89}$	$2.56^{+0.26}_{-0.24}$	$2.67^{+0.50}_{-0.63}$...	$5.30^{+0.99}_{-0.47}$	$0.77^{+0.10}_{-0.12}$	2.03 ± 0.04	$2.00^{+0.49}_{-0.47}$	$2.00^{+0.23}_{-0.23}$	$0.19^{+0.02}_{-0.01}$...	554.8/534
IC 4518A	8.78	$6.7^{+2.5}_{-1.9}$	$0.71^{+0.18}_{-0.14}$	$20.25^{+0.97}_{-0.93}$	$3.53^{+1.09}_{-0.93}$	$2.11^{+0.09}_{-0.08}$	$0.66^{+0.27}_{-0.18}$	$2.00^{+0.22}_{-0.22}$	$0.24^{+0.04}_{-0.05}$	$1.06^{+0.21}_{-0.12}$	234.1/212
LEDA 170194	3.00	$2.27^{+0.23}_{-0.24}$	$0.92^{+0.08}_{-0.06}$	$5.24^{+0.10}_{-0.12}$	$1.57^{+0.02}_{-0.03}$	$1.84^{+0.22}_{-0.18}$	$0.00^{+0.65}_{-0.00}$	738.4/643
MCG +04-48-002	20.7	$3.38^{+0.95}_{-0.74}$	$0.95^{+0.12}_{-0.10}$	$73.5^{+6.9}_{-8.4}$	26^{+152}_{-13}	$1.62^{+0.06}_{-0.05}$	$0.97^{+0.30}_{-0.25}$	$0.81^{+0.50}_{-0.35}$	$1.01^{+0.18}_{-0.28}$...	69.9/57
MCG -01-05-047	2.72	$2.41^{+1.26}_{-0.83}$	$0.50^{+0.16}_{-0.11}$	$18.4^{+1.4}_{-1.2}$	1.88 ± 0.11	$2.65^{+1.37}_{-0.92}$	$1.13^{+0.72}_{-0.50}$	110.0/87
MCG -02-08-014	4.46	$3.7^{+1.2}_{-1.0}$	$1.04^{+0.22}_{-0.18}$	$11.90^{+0.63}_{-0.64}$	$2.00^{+0.08}_{-0.10}$	$0.00^{+0.63}_{-0.00}$	$1.58^{+0.42}_{-0.64}$	178.9/160
MCG -05-23-016	8.70	$36.1^{+1.4}_{-1.5}$	$1.29^{+0.04}_{-0.03}$	1.57 ± 0.01	...	50.6 ± 3.0	0.27 ± 0.02	$1.96^{+0.02}_{-0.01}$	$0.47^{+0.04}_{-0.03}$	0.84 ± 0.12	3845.9/3479
Mrk 1210	3.45	$3.75^{+1.01}_{-0.72}$	$1.04^{+0.11}_{-0.14}$	$43.9^{+2.1}_{-2.0}$	1.80 ± 0.04	$0.70^{+0.31}_{-0.24}$	$1.81^{+0.35}_{-0.35}$	0.27 ± 0.03	$1.11^{+0.08}_{-0.07}$	193.8/158
Mrk 1498	1.83	$2.97^{+0.68}_{-0.30}$	$1.64^{+0.18}_{-0.23}$	$14.85^{+0.54}_{-0.45}$	$1.81^{+0.06}_{-0.05}$	$1.59^{+0.39}_{-0.31}$	$2.00^{+0.52}_{-0.52}$	$0.14^{+0.08}_{-0.06}$...	183.4/168
Mrk 18	4.37	$0.40^{+0.37}_{-0.29}$	$1.12^{+1.18}_{-0.46}$	$10.6^{+1.6}_{-1.3}$	$1.62^{+0.26}_{-0.26}$	$5.2^{+12.7}_{-3.3}$	$1.18^{+0.12}_{-1.18}$	40.4/34
Mrk 348	5.79	$11.94^{+0.26}_{-0.14}$	$1.40^{+0.03}_{-0.04}$	$6.01^{+0.11}_{-0.05}$...	$7.64^{+0.83}_{-0.66}$	$0.60^{+0.00}_{-0.02}$	$1.77^{+0.01}_{-0.01}$	$0.13^{+0.05}_{-0.04}$	$0.93^{+0.12}_{-0.13}$	$0.85^{+0.10}_{-0.08}$...	1699.4/1767
Mrk 417	1.88	$0.94^{+0.40}_{-0.30}$	$2.39^{+0.30}_{-0.51}$	44.9 ± 3.2	$1.60^{+0.08}_{-0.09}$	$0.78^{+0.84}_{-0.59}$	$1.76^{+0.24}_{-0.77}$	$1.04^{+0.20}_{-0.23}$...	74.3/70
Mrk 520	4.30	$1.63^{+0.16}_{-0.14}$	$1.25^{+0.11}_{-0.07}$	$1.87^{+0.04}_{-0.05}$	$1.53^{+0.02}_{-0.01}$	$5.27^{+0.59}_{-0.54}$	$0.00^{+0.13}_{-0.00}$	699.6/688
Mrk 915	5.35	$0.60^{+0.13}_{-0.11}$	$1.28^{+0.22}_{-0.18}$	1.59 ± 0.11	1.40 ± 0.03	$44.1^{+10.1}_{-7.8}$	$0.00^{+0.20}_{-0.00}$	304.5/277
NGC 1052	2.83	$2.41^{+0.32}_{-0.37}$	1.21 ± 0.14	$4.86^{+0.29}_{-0.16}$...	$19.8^{+2.5}_{-2.6}$	$0.71^{+0.02}_{-0.01}$	$1.75^{+0.06}_{-0.04}$	$4.81^{+0.29}_{-0.80}$	$0.35^{+0.28}_{-0.32}$	0.82 ± 0.05	...	416.1/425
NGC 1142	5.81	$4.48^{+0.74}_{-0.64}$	0.96 ± 0.07	$60.9^{+2.4}_{-2.2}$	$7.0^{+2.5}_{-2.3}$	1.66 ± 0.04	$0.25^{+0.09}_{-0.08}$	$0.78^{+0.22}_{-0.17}$	0.19 ± 0.07	0.97 ± 0.05	200.6/204
NGC 2110	2.18	18.70 ± 0.42	1.74 ± 0.04	$2.32^{+0.07}_{-0.06}$...	2.80 ± 0.09	0.64 ± 0.03	1.65 ± 0.01	0.28 ± 0.04	0.38 ± 0.06	0.98 ± 0.02	...	4276.3/3823
NGC 235A	1.41	$5.0^{+1.8}_{-1.3}$	$0.61^{+0.10}_{-0.09}$	$65.2^{+7.0}_{-6.3}$	$1.78^{+0.07}_{-0.08}$	$0.51^{+0.23}_{-0.18}$	$0.34^{+0.16}_{-0.14}$	$0.59^{+0.07}_{-0.08}$...	37.8/28
NGC 3081	3.88	$7.6^{+1.6}_{-1.3}$	0.72 ± 0.05	$82.5^{+4.0}_{-3.8}$	1.73 ± 0.05	$0.52^{+0.13}_{-0.10}$	$0.20^{+0.05}_{-0.06}$	$0.19^{+0.01}_{-0.02}$	0.98 ± 0.08	80.1/69
NGC 3431	4.17	$0.52^{+0.26}_{-0.12}$	$3.01^{+0.68}_{-1.05}$	$7.08^{+0.28}_{-0.29}$	$1.61^{+0.02}_{-0.07}$	$1.42^{+0.78}_{-0.75}$	$2.0^{+1.3}_{-1.3}$	245.9/234
NGC 4388	2.58	19.2 ± 1.1	$0.88^{+0.01}_{-0.02}$	$23.78^{+0.69}_{-0.70}$...	43.1 ± 3.6	0.56 ± 0.03	1.65 ± 0.01	$0.65^{+0.04}_{-0.03}$	$0.08^{+0.05}_{-0.04}$	$0.24^{+0.01}_{-0.02}$	0.97 ± 0.02	1669.1/1703
NGC 4507	7.04	$19.7^{+2.5}_{-2.3}$	$0.57^{+0.03}_{-0.02}$	$26.9^{+5.2}_{-3.9}$...	$79.9^{+5.1}_{-5.7}$	0.91 ± 0.02	$1.79^{+0.03}_{-0.02}$	$0.31^{+0.05}_{-0.04}$	$0.43^{+0.08}_{-0.07}$	0.15 ± 0.01	0.81 ± 0.02	387.0/360
NGC 4992	1.93	$2.17^{+0.65}_{-0.51}$	$1.05^{+0.15}_{-0.13}$	$60.1^{+3.6}_{-3.4}$	1.57 ± 0.06	$0.00^{+0.17}_{-0.00}$	$0.52^{+0.18}_{-0.13}$	74.0/61
NGC 5252	2.14	$8.88^{+0.87}_{-0.77}$	0.47 ± 0.02	$2.11^{+0.53}_{-0.52}$...	$5.86^{+0.36}_{-0.33}$	$0.81^{+0.05}_{-0.06}$	$1.66^{+0.03}_{-0.02}$	$0.39^{+0.24}_{-0.24}$	$0.00^{+0.02}_{-0.02}$	0.16 ± 0.02	$0.84^{+0.06}_{-0.05}$	472.6/443
NGC 526A	2.31	3.12 ± 0.39	$3.78^{+0.58}_{-0.43}$	1.22 ± 0.01	1.68 ± 0.01	$6.46^{+0.71}_{-0.84}$	$0.99^{+0.43}_{-0.33}$	2467.0/2335

TABLE A — Continued

Target Name (1)	$N_{\text{H}}^{\text{Gal}}$ (2)	A_{pl} (3)	N_{XIS} (4)	N_{H} (5)	$N_{\text{H}}^{\text{ref}}$ (6)	N_{H}^{pc} (7)	f_{pc} (8)	Γ (9)	f_{scat} (10)	R (11)	kT_1 (12)	kT_2 (13)	χ^2/dof (14)
NGC 5506	4.08	$26.29^{+0.83}_{-0.59}$	1.73 ± 0.03	$3.10^{+0.01}_{-0.02}$	$1.95^{+0.00}_{-0.01}$	$1.09^{+0.04}_{-0.05}$	$2.00^{+0.00}_{-0.07}$	3398.7/3185
NGC 6300	7.79	$11.43^{+1.00}_{-0.93}$	$1.04^{+0.06}_{-0.05}$	$22.21^{+0.35}_{-0.34}$	1.86 ± 0.02	0.56 ± 0.08	$0.83^{+0.12}_{-0.10}$	$0.85^{+0.06}_{-0.07}$...	765.9/723
NGC 7172	1.95	$14.18^{+0.53}_{-0.51}$	$1.44^{+0.04}_{-0.05}$	8.90 ± 0.07	$1.74^{+0.01}_{-0.02}$	0.12 ± 0.03	$0.34^{+0.10}_{-0.09}$	$0.33^{+0.14}_{-0.04}$...	2056.7/2033
NGC 788	2.12	$5.35^{+1.16}_{-0.99}$	$1.19^{+0.13}_{-0.11}$	$73.4^{+4.0}_{-3.8}$	$11.9^{+3.4}_{-3.1}$	1.77 ± 0.05	$0.71^{+0.19}_{-0.14}$	$1.21^{+0.48}_{-0.35}$	$0.75^{+0.08}_{-0.11}$...	88.8/87
UGC 03142	17.6	$1.11^{+0.34}_{-0.17}$	$1.45^{+0.17}_{-0.26}$	$1.59^{+0.37}_{-0.32}$...	$9.67^{+0.94}_{-0.65}$	$0.79^{+0.01}_{-0.03}$	$1.58^{+0.07}_{-0.08}$	$3.92^{+0.81}_{-1.45}$	$2.00^{+0.77}_{-0.77}$	205.8/231
UGC 12741	5.79	$1.88^{+1.28}_{-0.80}$	$1.47^{+0.55}_{-0.33}$	$60.8^{+5.0}_{-4.7}$	$1.79^{+0.12}_{-0.11}$	$0.00^{+0.78}_{-0.78}$	$0.62^{+0.42}_{-0.24}$	52.5/41

NOTE. — (1) Galaxy name. (2) Galactic absorption in units of 10^{20} cm^{-2} . (3) Normalization of the cutoff power-law component at 1 keV in units of $10^{-3} \text{ photons keV}^{-1} \text{ cm}^{-2} \text{ s}^{-1}$. (4) Time variability of the cutoff power-law component between the *Suzaku* and *Swift*/BAT spectra. (5) Intrinsic absorption in units of 10^{22} cm^{-2} . (6) Absorption of the reflection components in units of 10^{22} cm^{-2} . (7) Partial absorption of the cutoff power-law component in units of 10^{22} cm^{-2} . (8) Covering fraction of the partial absorption of the cutoff power-law component. (9) Photon index of the cutoff power-law component. (10) Scattered fraction in units of %. (11) Relative reflection strength ($R = \Omega/2\pi$) of the pexrav model. (12)–(13) Temperatures of the `apec` models in units of keV. (14) Chi squared and degrees of freedom.

TABLE B
 FLUX AND LUMINOSITY

Target Name (1)	$\log F_{0.5-2}^{\text{BI-XIS}}$ (2)	$\log F_{2-10}^{\text{FI-XIS}}$ (3)	$\log F_{10-50}^{\text{PIN*}}$ (4)	$\log F_{10-50}^{\text{BAT}}$ (5)	$\log L_{0.5-2}^{\text{BI-XIS}}$ (6)	$\log L_{2-10}^{\text{FI-XIS}}$ (7)	$\log L_{10-50}^{\text{PIN*}}$ (8)	$\log L_{10-50}^{\text{BAT}}$ (9)	EW (10)	$L_{\text{K}\alpha}/L_{10-50}^{\text{BAT}}$ (11)	$\lambda_{\text{Edd}}^{\text{Suzaku}}/\lambda_{\text{Edd}}^{\text{BAT}}$ (12)
2MASX J0216+5126	-12.2	-11.1	-11.0	-11.0	43.0	43.2	43.3	43.3	35^{+13}_{-12}	$2.58^{+0.93}_{-0.86}$.../...
2MASX J0248+2630	-13.4	-11.3	-10.6	-10.9	43.5	43.9	44.3	44.1	61 ± 16	3.56 ± 0.91	.../...
2MASX J0318+6829	-13.3	-11.4	-10.9	-11.1	43.7	44.1	44.4	44.2	42^{+13}_{-12}	$3.08^{+0.92}_{-0.89}$.../...
2MASX J0350-5018	-13.1	-12.1	-11.1	-11.1	42.3	42.7	43.4	43.4	376^{+65}_{-61}	$5.97^{+1.03}_{-0.96}$	-2.8/-2.7
2MASX J0444+2813	-13.6	-11.3	-10.7	-10.6	41.7	42.1	42.6	42.6	119 ± 13	3.82 ± 0.40	-2.0/-2.0
2MASX J0505-2351	-12.8	-11.0	-10.6	-10.5	43.4	43.7	43.9	43.9	60 ± 6	2.96 ± 0.31	-0.7/-0.6
2MASX J0911+4528	-14.2	-11.7	-11.1	-11.0	43.2	43.2	43.2	43.3	43 ± 15	1.67 ± 0.57	-1.2/-1.0
2MASX J1200+0648	-13.5	-11.1	-10.7	-10.9	43.4	43.6	43.8	43.6	57^{+9}_{-8}	$5.67^{+0.88}_{-0.76}$	-1.7/-2.1
Ark 347	-12.9	-12.0	-11.0	-10.9	42.0	42.4	43.0	43.2	149 ± 46	2.43 ± 0.74	-2.5/-2.2
ESO 103-035	-13.1	-10.6	-10.1	-10.1	43.5	43.5	43.6	43.5	52 ± 5	3.50 ± 0.36	-0.8/-0.9
ESO 263-G013	-13.2	-11.4	-10.8	-10.8	43.2	43.4	43.7	43.7	85 ± 16	3.35 ± 0.64	-1.3/-1.3
ESO 297-G018	-13.5	-11.5	-10.5	-10.5	43.2	43.5	43.7	43.7	154 ± 23	3.14 ± 0.47	-3.0/-3.0
ESO 506-G027	-13.3	-11.7	-10.6	-10.4	43.1	43.3	43.6	43.8	465^{+33}_{-32}	4.26 ± 0.30	-2.0/-1.8
Fairall 49	-11.3	-10.6	-10.7	-10.9	43.5	43.4	43.3	43.0	49 ± 6	10.3 ± 1.2	.../...
Fairall 51	-12.1	-10.7	-10.3	-10.6	42.9	42.9	43.1	42.8	40 ± 8	$5.21^{+1.03}_{-0.98}$	-1.8/-2.2
IC 4518A	-12.8	-11.3	-10.7	-10.7	42.8	42.8	43.0	43.1	56 ± 17	$2.53^{+0.77}_{-0.76}$	-1.5/-1.3
LEDA 170194	-12.9	-11.2	-10.7	-10.7	43.1	43.5	43.8	43.8	66^{+8}_{-7}	$3.30^{+0.40}_{-0.36}$	-2.2/-2.2
MCG +04-48-002	-13.1	-11.7	-10.5	-10.5	42.5	42.8	43.2	43.2	183^{+2590}_{-46}	$4.0^{+57.1}_{-1.0}$	-1.2/-1.1
MCG -01-05-047	-12.9	-11.7	-11.0	-10.9	42.2	42.4	42.7	42.9	221 ± 26	6.07 ± 0.71	-2.0/-1.7
MCG -02-08-014	-13.7	-11.3	-10.8	-10.8	42.7	42.8	43.0	43.0	117 ± 15	6.77 ± 0.85	.../...
MCG -05-23-016	-11.1	-10.1	-9.8	-9.9	43.2	43.3	43.4	43.3	58 ± 3	4.65 ± 0.22	-0.9/-1.0
Mrk 1210	-12.6	-11.3	-10.5	-10.5	42.6	42.8	43.1	43.1	190 ± 15	5.15 ± 0.40	-1.9/-1.9
Mrk 1498	-12.3	-11.1	-10.5	-10.6	43.9	44.1	44.4	44.3	72 ± 12	4.00 ± 0.68	-1.3/-1.5
Mrk 18	-13.4	-11.8	-11.3	-11.3	41.4	41.8	42.2	42.2	248^{+55}_{-56}	10.0 ± 2.2	-2.4/-2.5
Mrk 348	-12.7	-10.5	-10.0	-10.1	43.3	43.5	43.7	43.6	45^{+4}_{-5}	$2.93^{+0.25}_{-0.30}$	-1.3/-1.4
Mrk 417	-13.3	-11.5	-10.6	-10.8	43.1	43.4	43.8	43.6	125 ± 21	4.72 ± 0.78	-1.4/-1.8
Mrk 520	-12.2	-11.1	-10.7	-10.8	42.8	43.1	43.5	43.4	92 ± 9	$6.20^{+0.62}_{-0.59}$	-2.0/-2.1
Mrk 915	-12.1	-11.2	-10.8	-10.9	42.5	42.9	43.3	43.2	133^{+18}_{-17}	$7.39^{+1.01}_{-0.93}$	-2.0/-2.0
NGC 1052	-12.5	-11.3	-10.8	-10.8	41.5	41.7	41.9	41.9	114 ± 10	$6.63^{+0.58}_{-0.60}$	-3.7/-3.8
NGC 1142	-13.0	-11.4	-10.4	-10.4	43.2	43.6	43.9	43.9	226^{+16}_{-15}	$4.66^{+0.33}_{-0.31}$	-2.5/-2.5
NGC 2110	-11.6	-10.0	-9.6	-9.8	43.0	43.3	43.6	43.4	34 ± 2	3.04 ± 0.17	-1.7/-2.0
NGC 235A	-12.8	-11.7	-10.8	-10.6	42.9	43.1	43.3	43.5	171 ± 69	2.7 ± 1.1	-2.5/-2.3
NGC 3081	-12.6	-11.5	-10.5	-10.4	42.0	42.3	42.5	42.6	313 ± 25	3.90 ± 0.31	-2.2/-2.1
NGC 3431	-13.5	-11.3	-10.8	-11.1	42.4	42.7	43.1	42.8	102 ± 13	8.4 ± 1.1	.../...
NGC 4388	-12.3	-10.7	-9.9	-9.9	42.3	42.6	42.8	42.9	190 ± 5	4.92 ± 0.12	-2.2/-2.2
NGC 4507	-12.3	-11.2	-10.2	-10.0	42.9	43.1	43.3	43.5	421 ± 14	4.30 ± 0.15	-1.7/-1.5
NGC 4992	-14.3	-11.6	-10.6	-10.2	42.8	43.3	43.6	43.6	168 ± 30	3.17 ± 0.57	-2.0/-2.1
NGC 5252	-12.4	-11.0	-10.6	-10.2	42.9	43.1	43.4	43.7	83^{+10}_{-9}	$2.29^{+0.28}_{-0.24}$	-2.5/-2.2
NGC 526A	-11.3	-10.4	-10.1	-10.5	43.3	43.6	43.9	43.4	48 ± 4	7.85 ± 0.67	-1.2/-1.7
NGC 5506	-11.4	-10.0	-9.7	-9.8	42.8	43.0	43.1	43.0	44^{+4}_{-2}	$3.87^{+0.32}_{-0.22}$	-1.3/-1.5

Kawamuro et al.

TABLE B — Continued

Target Name (1)	$\log F_{0.5-2}^{\text{BI-XIS}}$ (2)	$\log F_{2-10}^{\text{FI-XIS}}$ (3)	$\log F_{10-50}^{\text{PIN}*}$ (4)	$\log F_{10-50}^{\text{BAT}}$ (5)	$\log L_{0.5-2}^{\text{BI-XIS}}$ (6)	$\log L_{2-10}^{\text{FI-XIS}}$ (7)	$\log L_{10-50}^{\text{PIN}*}$ (8)	$\log L_{10-50}^{\text{BAT}}$ (9)	EW (10)	$L_{\text{K}\alpha}/L_{10-50}^{\text{BAT}}$ (11)	$\lambda_{\text{Edd}}^{\text{Suzaku}}/\lambda_{\text{Edd}}^{\text{BAT}}$ (12)
NGC 6300	-12.7	-10.8	-10.2	-10.2	41.8	42.0	42.2	42.1	67 ± 7	3.22 ± 0.33	-2.1/-2.2
NGC 7172	-12.8	-10.3	-9.9	-10.1	42.8	43.0	43.2	43.1	52 ± 4	4.04 ± 0.33	-1.7/-1.9
NGC 788	-12.9	-11.4	-10.4	-10.4	42.8	43.0	43.3	43.2	223^{+24}_{-22}	$5.45^{+0.58}_{-0.54}$	-2.0/-2.0
UGC 03142	-12.8	-11.3	-10.6	-10.7	42.6	42.9	43.4	43.3	156 ± 15	$6.24^{+0.60}_{-0.59}$	-2.1/-2.3
UGC 12741	-14.4	-11.8	-10.9	-11.0	42.6	42.8	43.0	42.9	150 ± 28	$4.96^{+0.92}_{-0.93}$.../...

NOTE. — (1) Galaxy name. (2)–(5) Logarithmic observed flux in the 0.5–2 keV (BI-XIS), 2–10 keV (FI-XISs), 10–50 keV (PIN), and 10–50 keV (BAT) bands in units of $\text{erg cm}^{-2} \text{ s}^{-1}$. (6)–(9) Logarithmic absorption-corrected luminosity in the same energy bands as (2)–(5) in units of erg s^{-1} , respectively. (10) Equivalent width of the iron-K α line in units of eV. (11) Ratio of the iron-K α line to 10–50 keV continuum luminosity in units of $\times 10^{-3}$. (12) Logarithmic Eddington ratio based on the 2–10 keV luminosity measured with *Suzaku* and *Swift*/BAT. * According to the XIS or HXD nominal position observation, the flux and luminosity are divided by 1.16 or 1.18 to take into account the instrumental cross-calibration factor between the FI-XISs and HXD/PIN spectra.

TABLE C
INFORMATION OF DETECTED EMISSION/ABSORPTION LINES

TABLE C — Continued

Target Name (1)	$N_{6.4 \text{ keV}}$ (2)	$N_{6.31 \text{ keV}}$ (3)	$N_{6.70 \text{ keV}}$ (4)	$N_{6.97 \text{ keV}}$ (5)	$N_{7.06 \text{ keV}}$ (6)	$N_{7.48 \text{ keV}}$ (7)	E_1 (8)	N_1 (9)	E_2 (10)	N_2 (11)	E_3 (12)	N_3 (13)	E_4 (14)	N_4 (15)
NGC 7172	36.5 ± 3.0	8.0 ± 2.9
NGC 788	$23.6^{+2.5}_{-2.3}$
UGC 03142	13.4 ± 1.3
UGC 12741	5.6 ± 1.1

NOTE. — (1) Galaxy name. (2)-(7) Normalization of the emission lines at 6.40 keV, 6.31 keV, 6.68 keV, 6.93 keV, 7.06 keV, and 7.48 keV in units of $\times 10^{-6}$ photons $\text{cm}^{-2} \text{ s}^{-1}$.

(8)-(13) Line Energy and normalization of emission/absorption lines in units of keV and $\times 10^{-6}$ photons $\text{cm}^{-2} \text{ s}^{-1}$, respectively.

SUZAKU OBSERVATIONS OF SWIFT/BAT SELECTED COMPTON-THIN AGNs

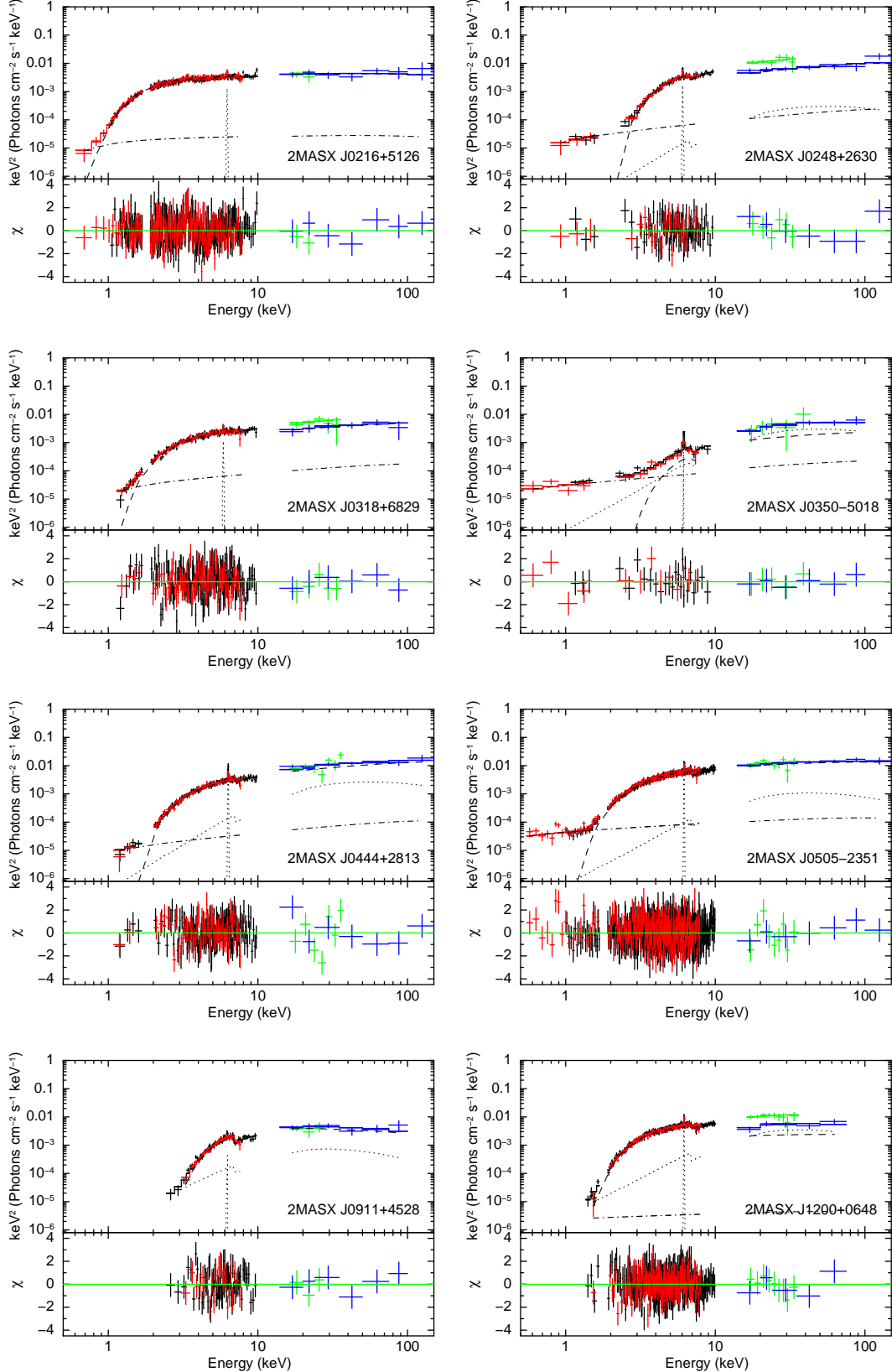


FIG. A.— Unfolded spectra and best-fitting models obtained in Section 3.1. The FI-XISs, BI-XIS, HXD/PIN and *Swift*/BAT spectra are represented with the black, red, green, and blue crosses in the upper panel, respectively, whereas the fit residuals in the lower panel. The solid, dashed, dotted, dot-dashed, and dot-dot-dashed lines correspond to the total, cutoff power-law component, reflection components (e.g., iron-K α emission line and reflection continuum), scattered component, and optically-thin thermal emission, respectively.

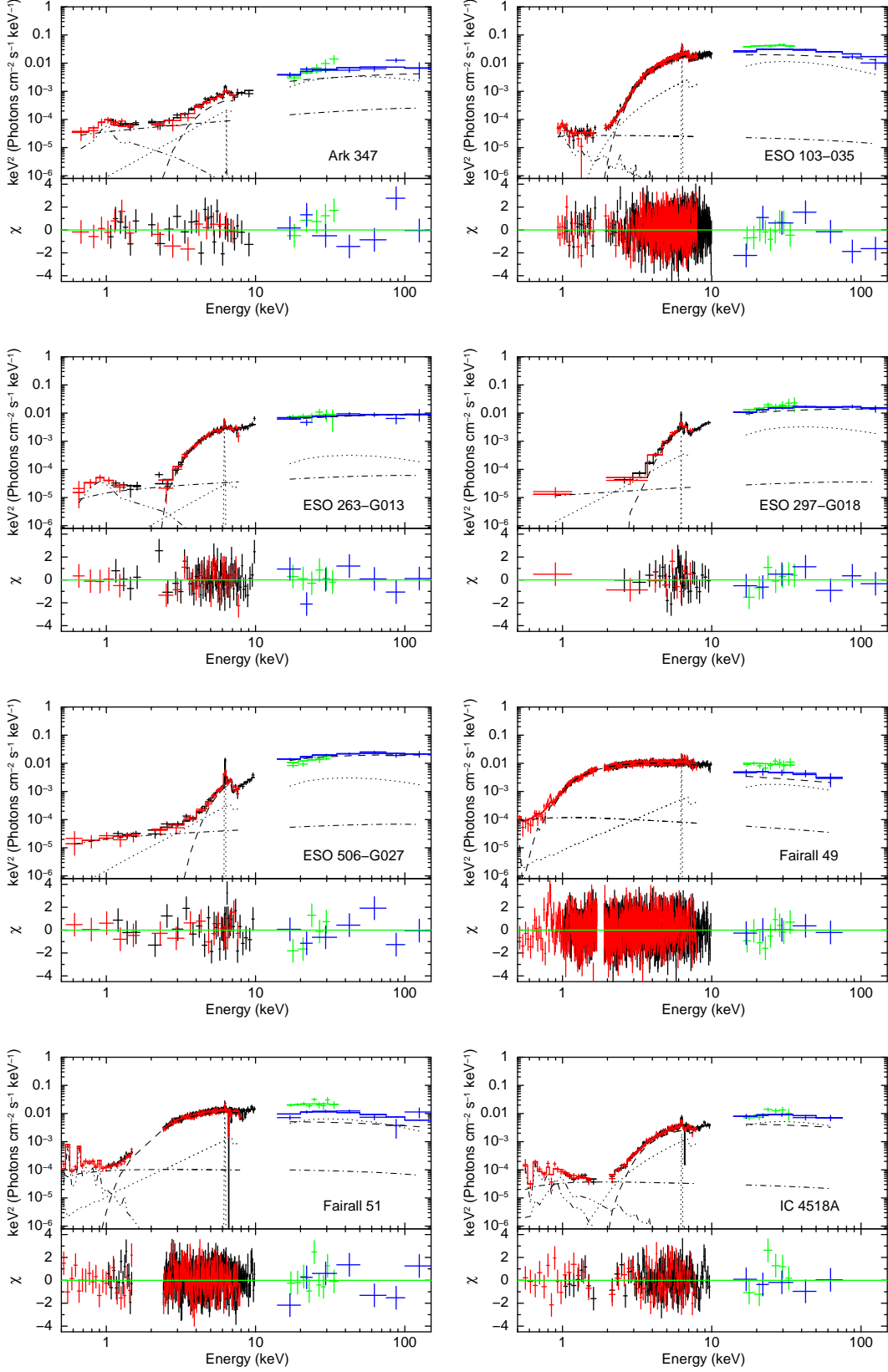


FIG. A.— Continued.

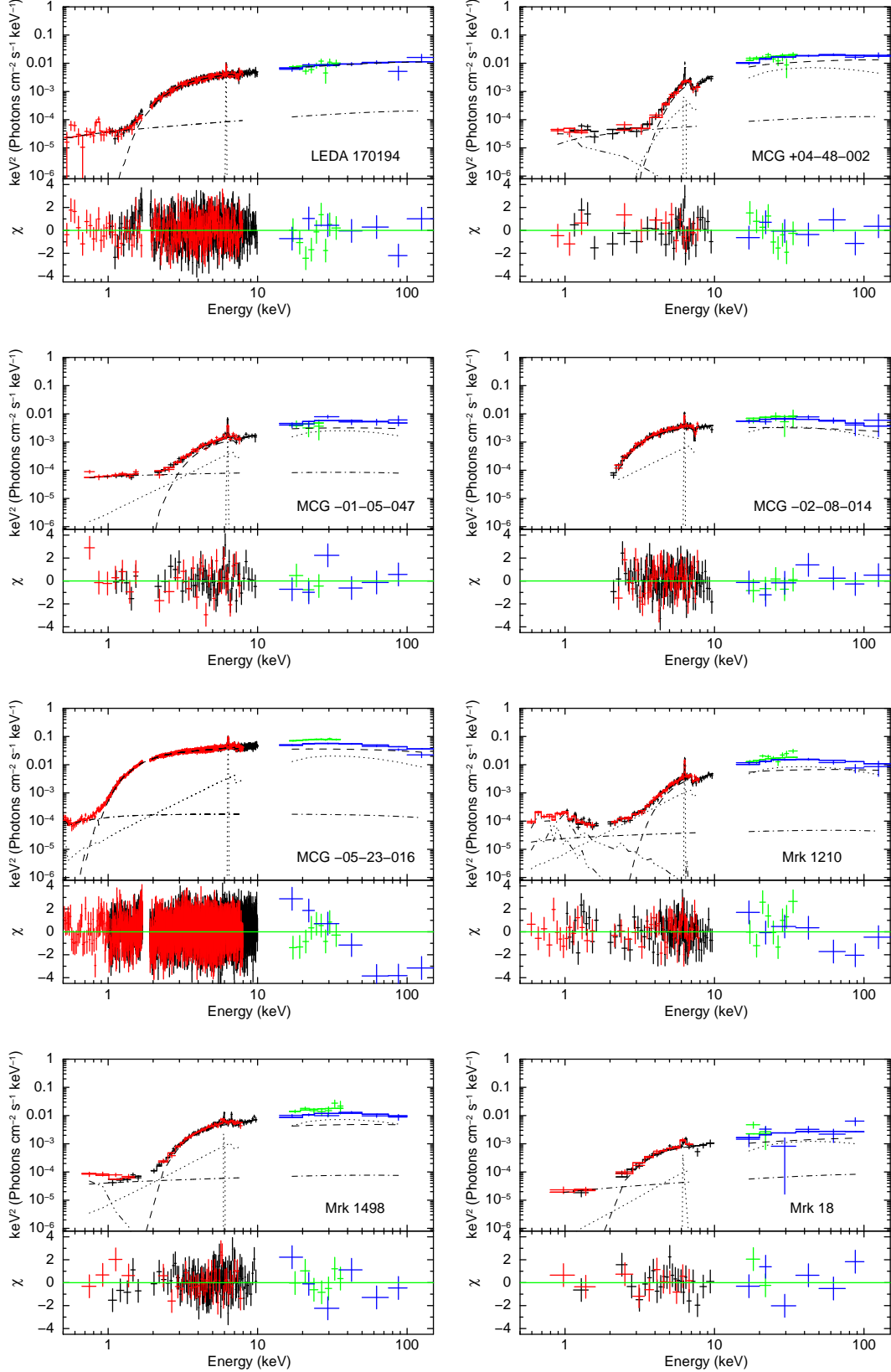


FIG. A.— Continued.

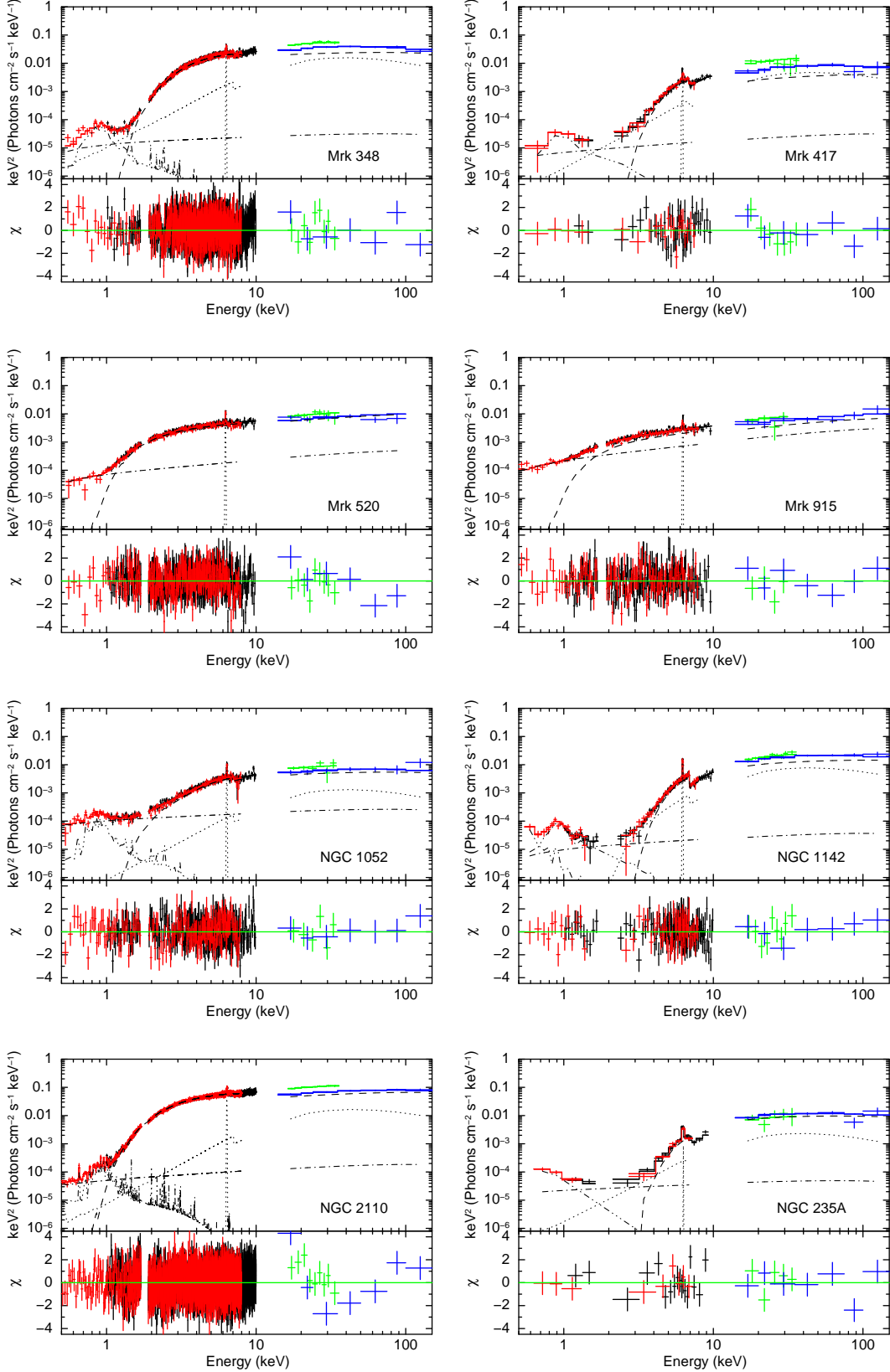


FIG. A.— Continued.

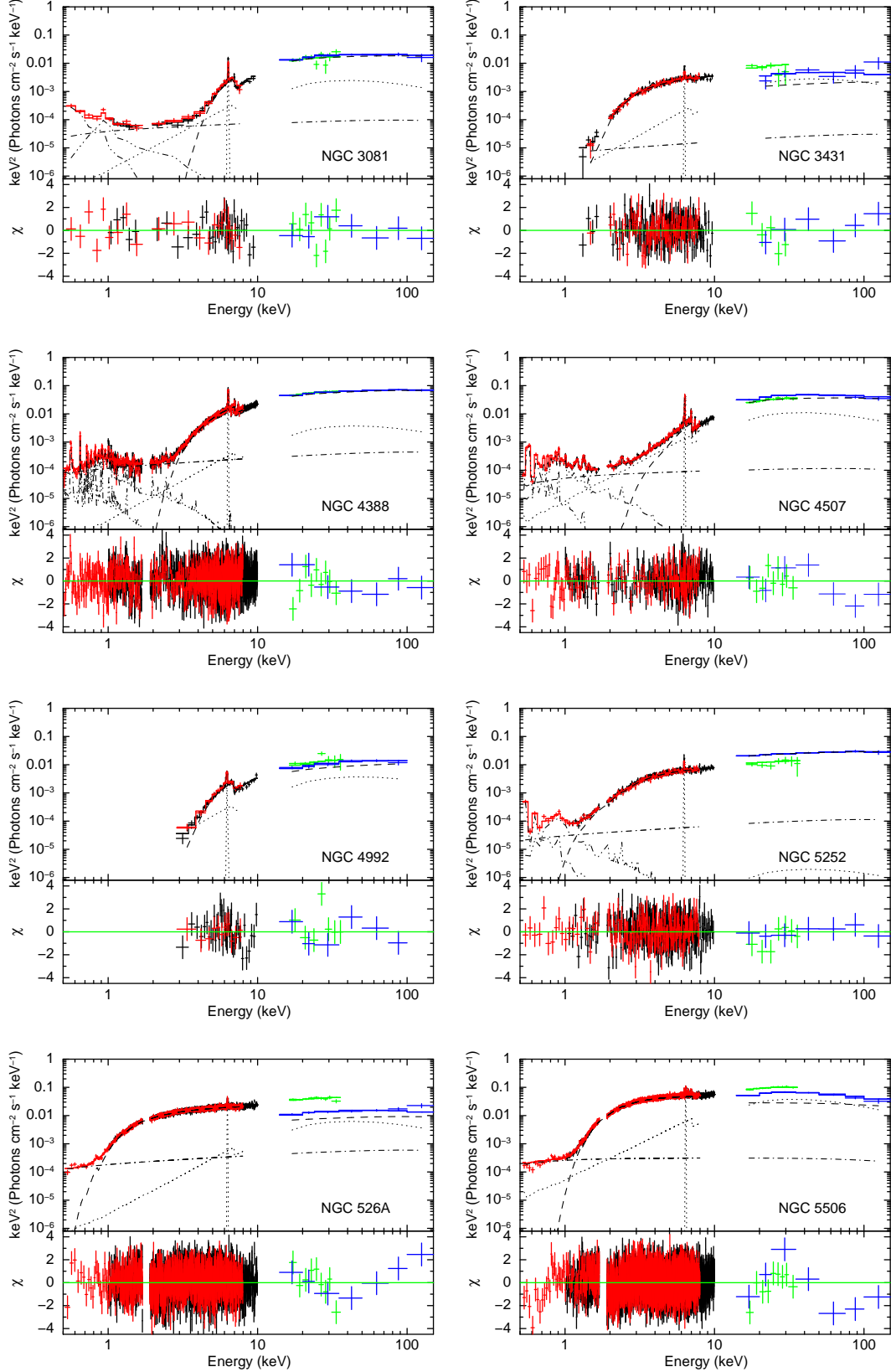


FIG. A.— Continued.

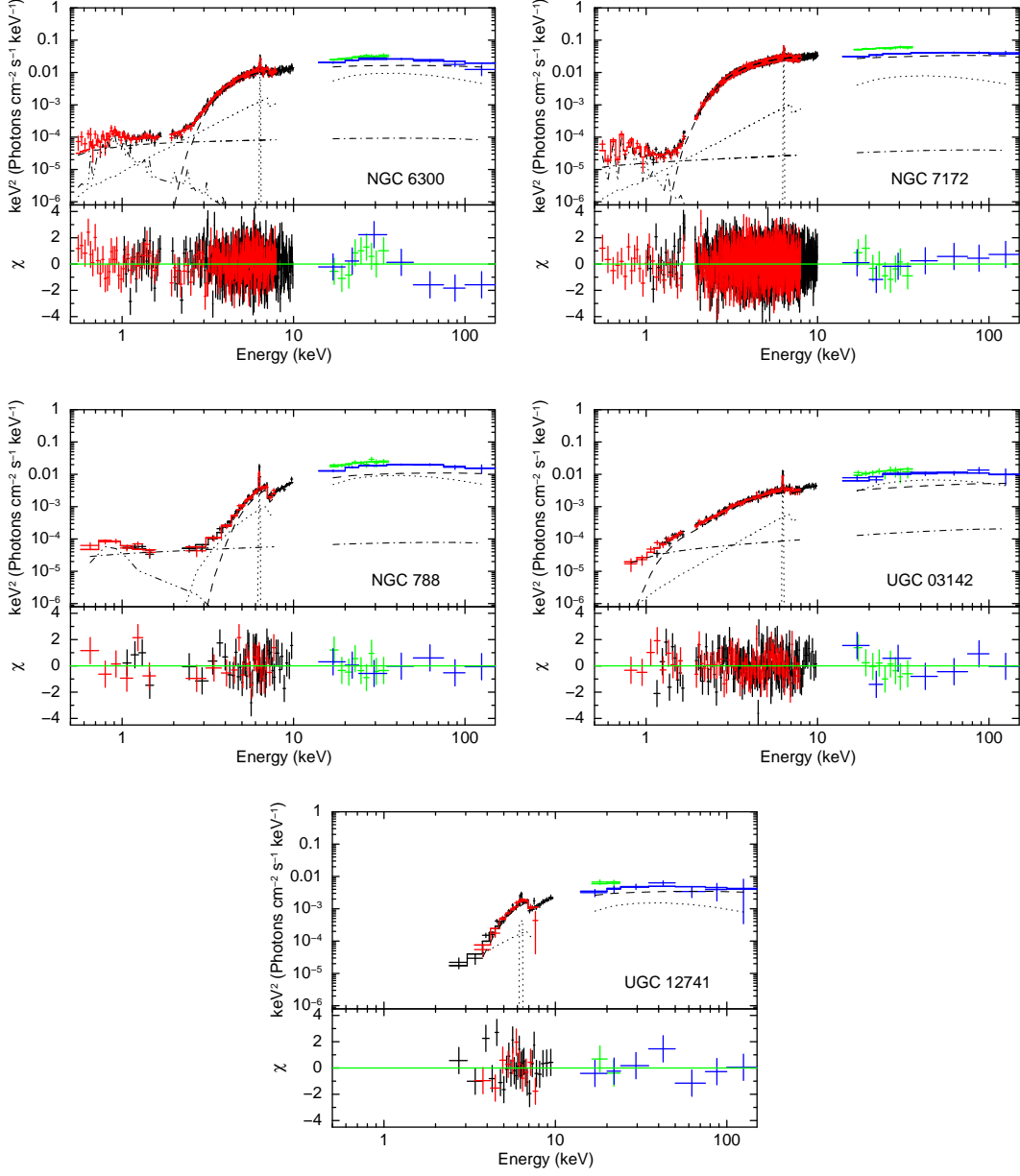


FIG. A.— Continued.

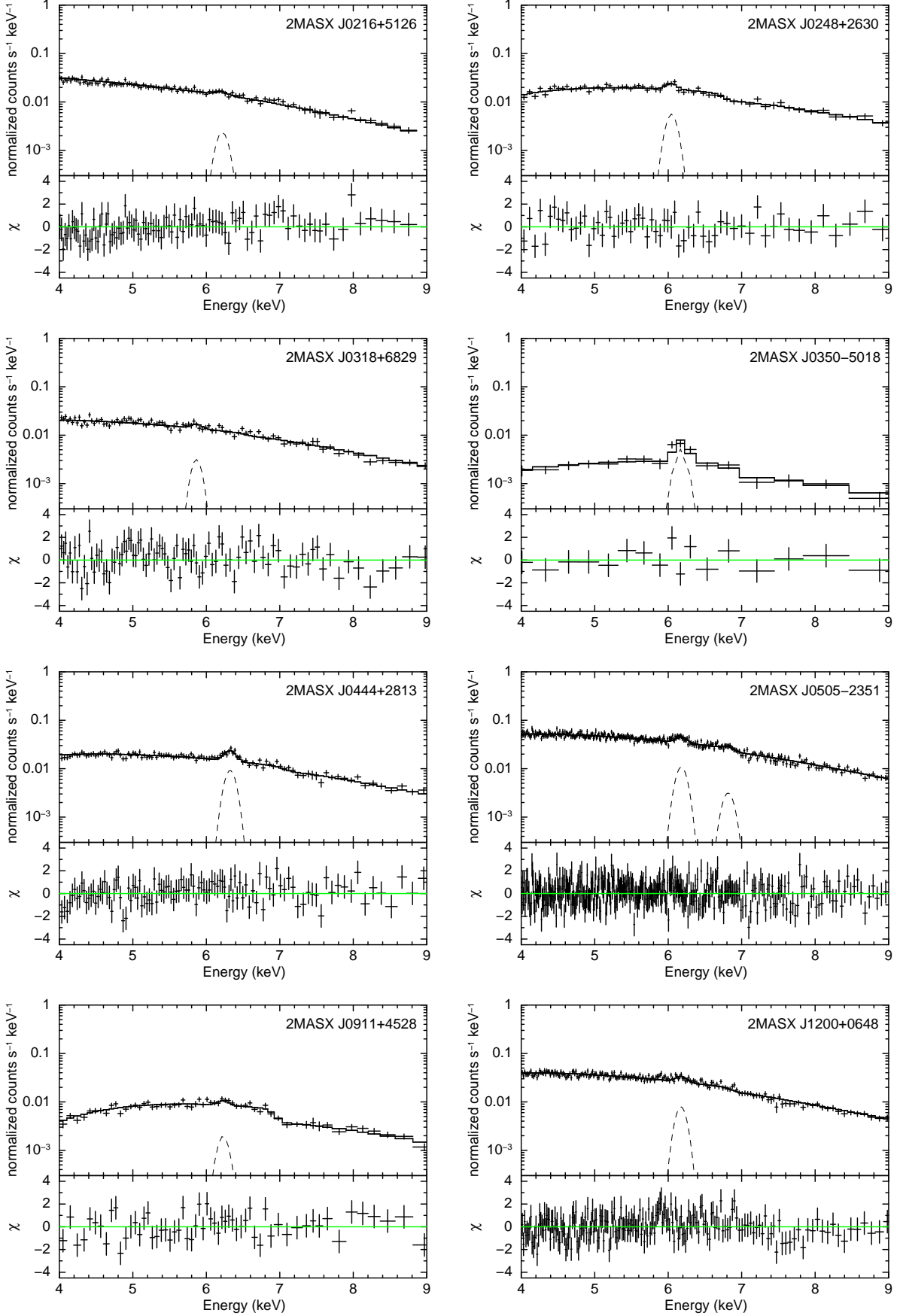


FIG. B.— Narrow band spectra and best-fitting models obtained in Section 3.1. The FI-XISs spectrum is represented with the black crosses in the upper panel, whereas the fit residuals in the lower panel. The solid and dashed lines correspond to the total and detected emission lines, respectively.

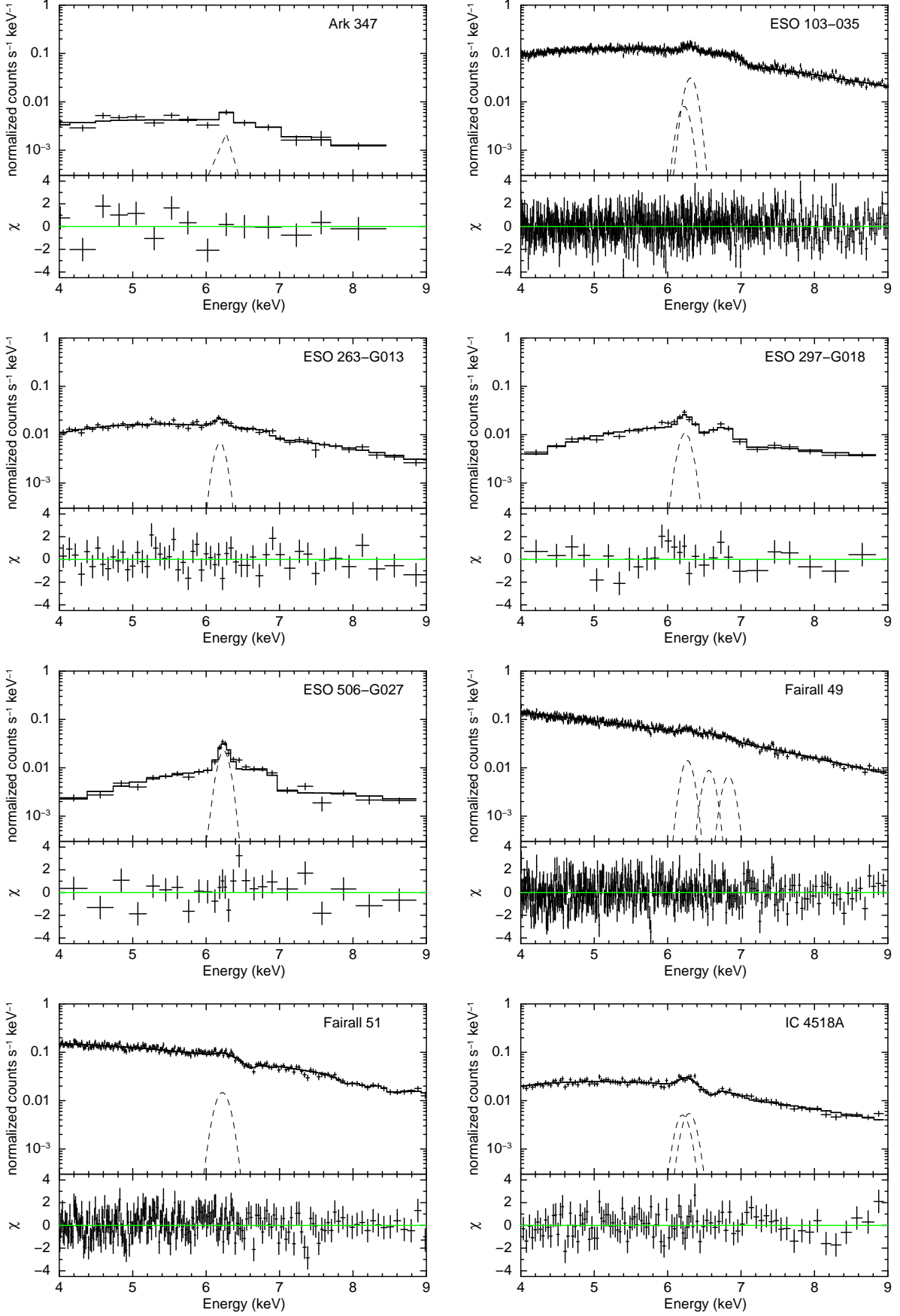


FIG. B.— Continued.

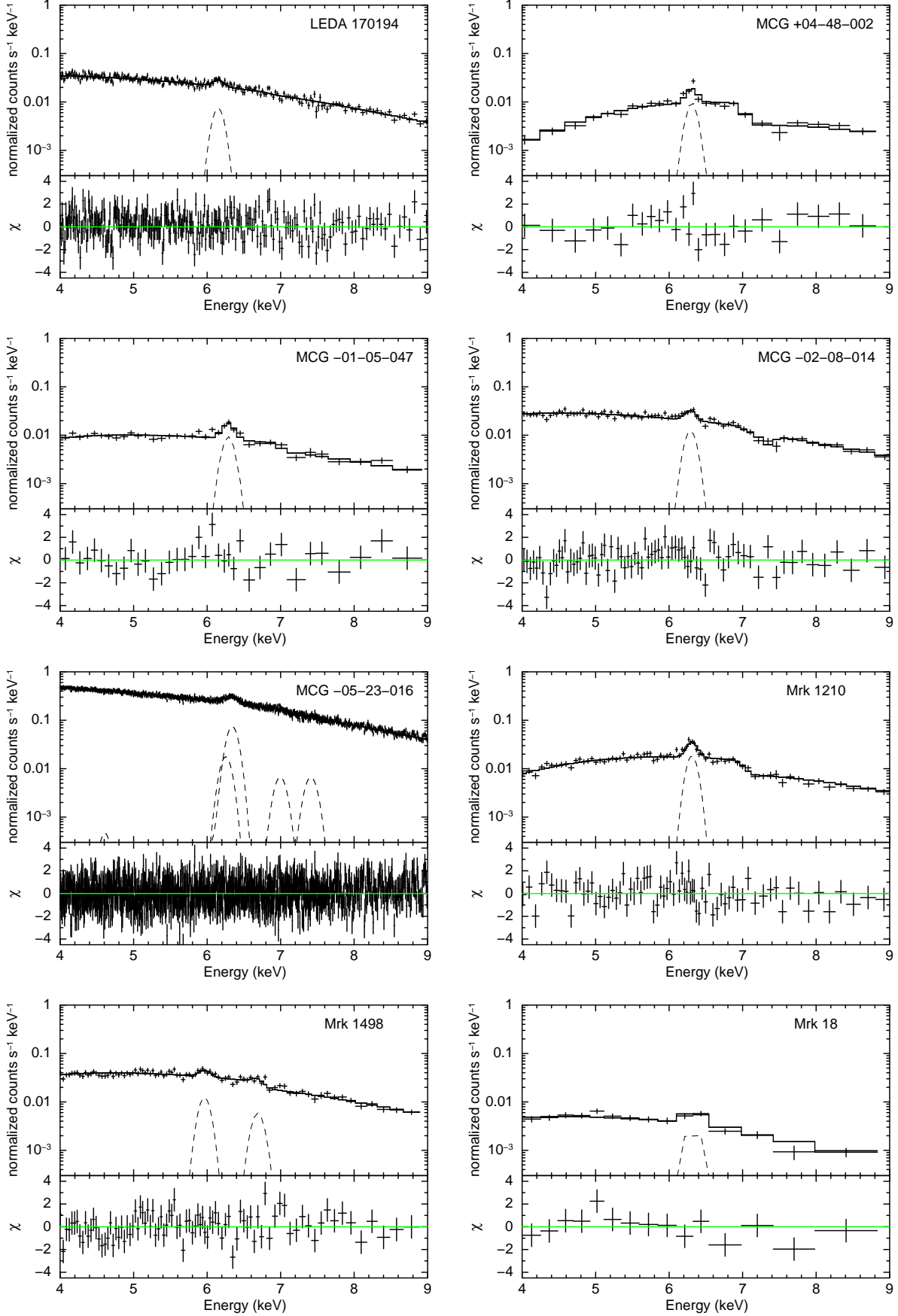


FIG. B.— Continued.

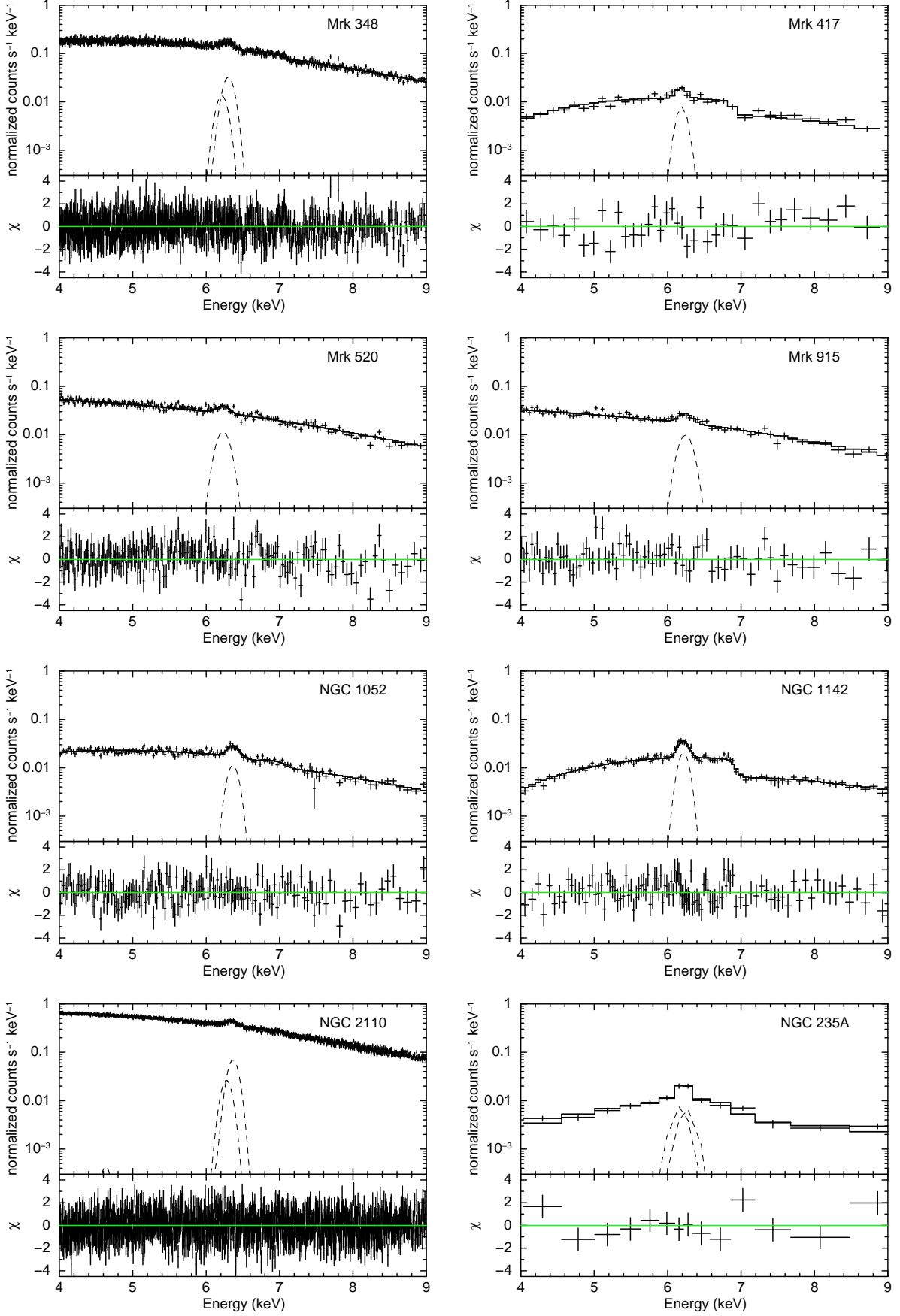


FIG. B.— Continued.

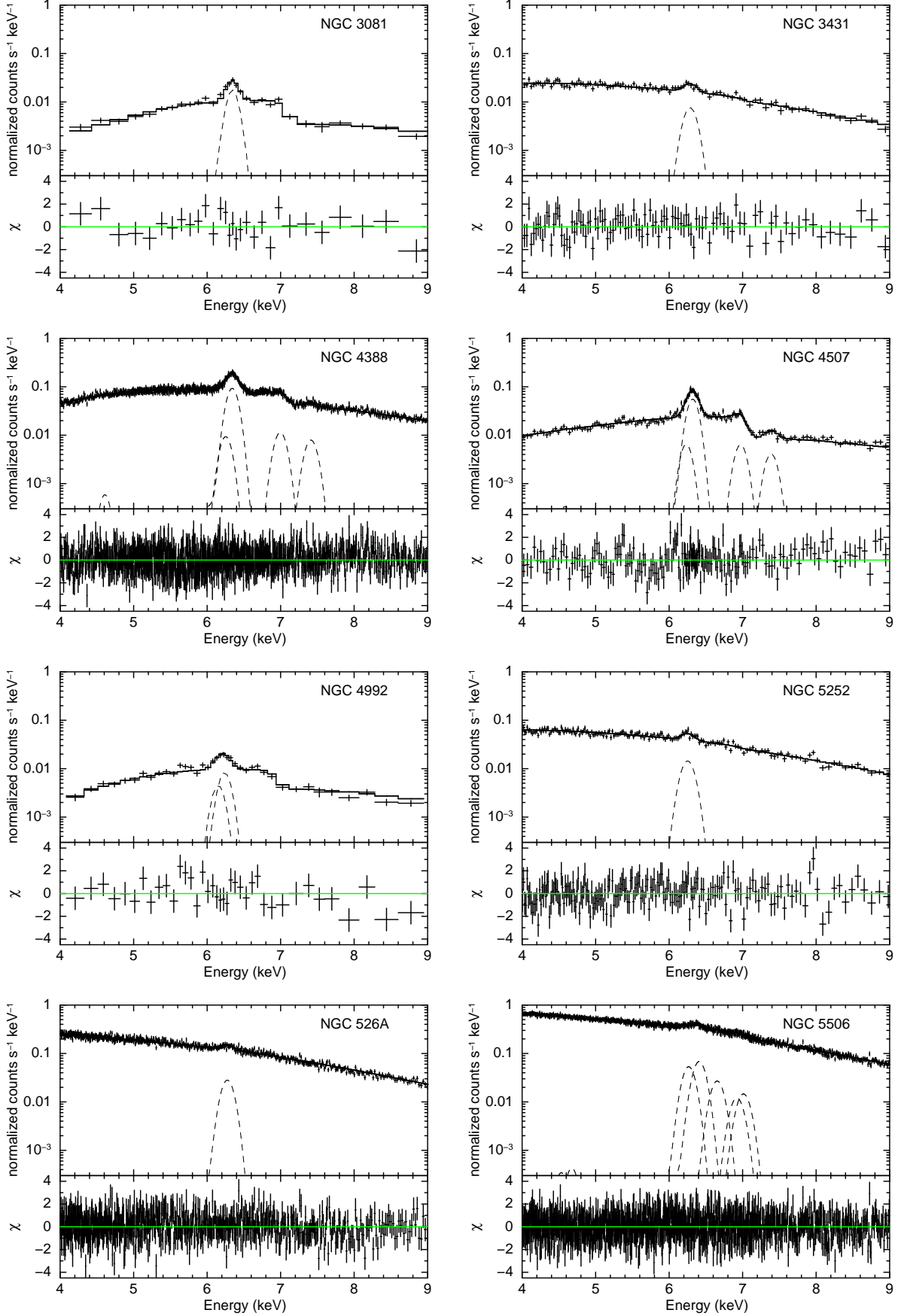


FIG. B.— Continued.

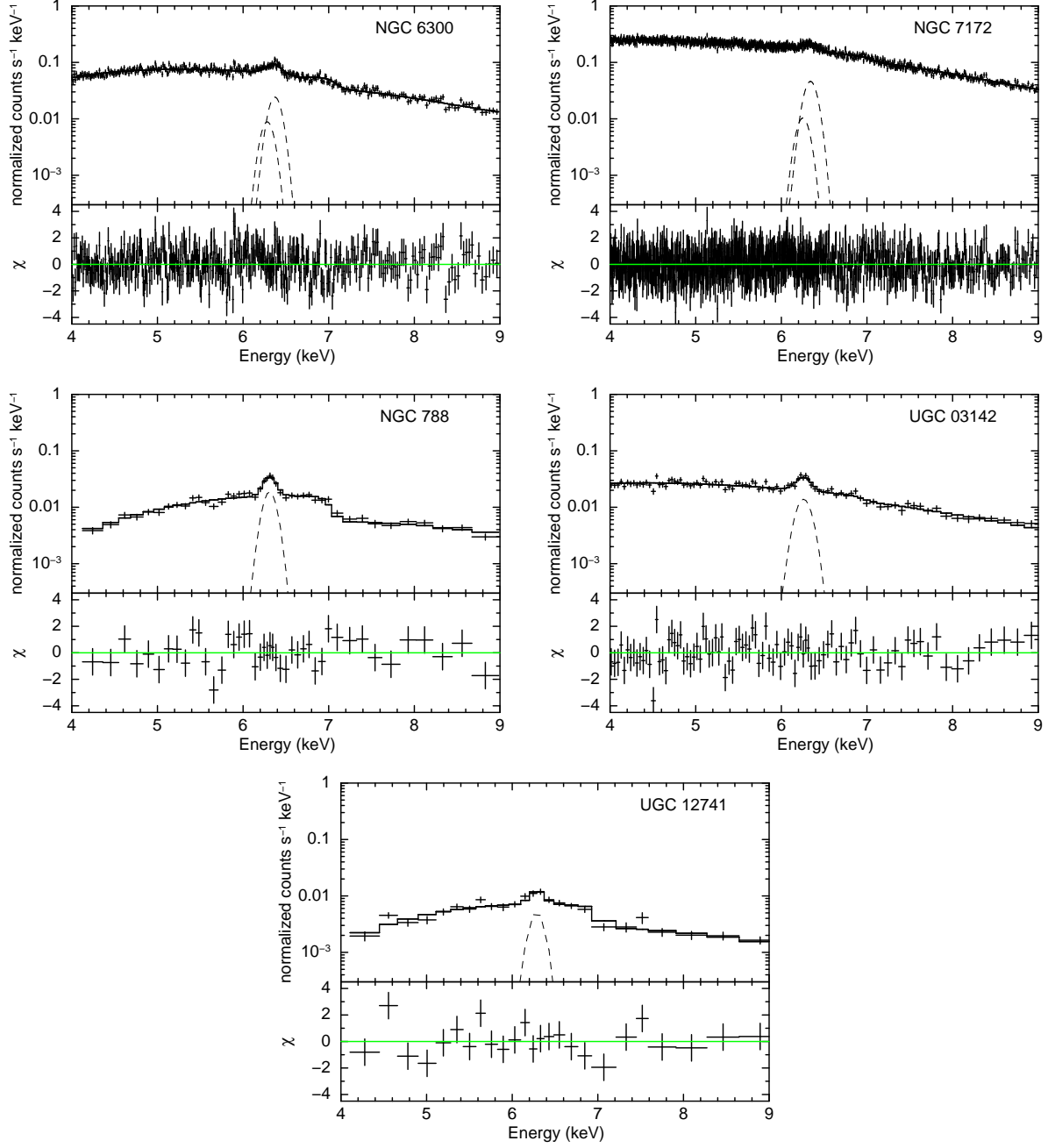


FIG. B.— Continued.

SPECTRA FITTED WITH THE RELATIVISTIC REFLECTION COMPONENT

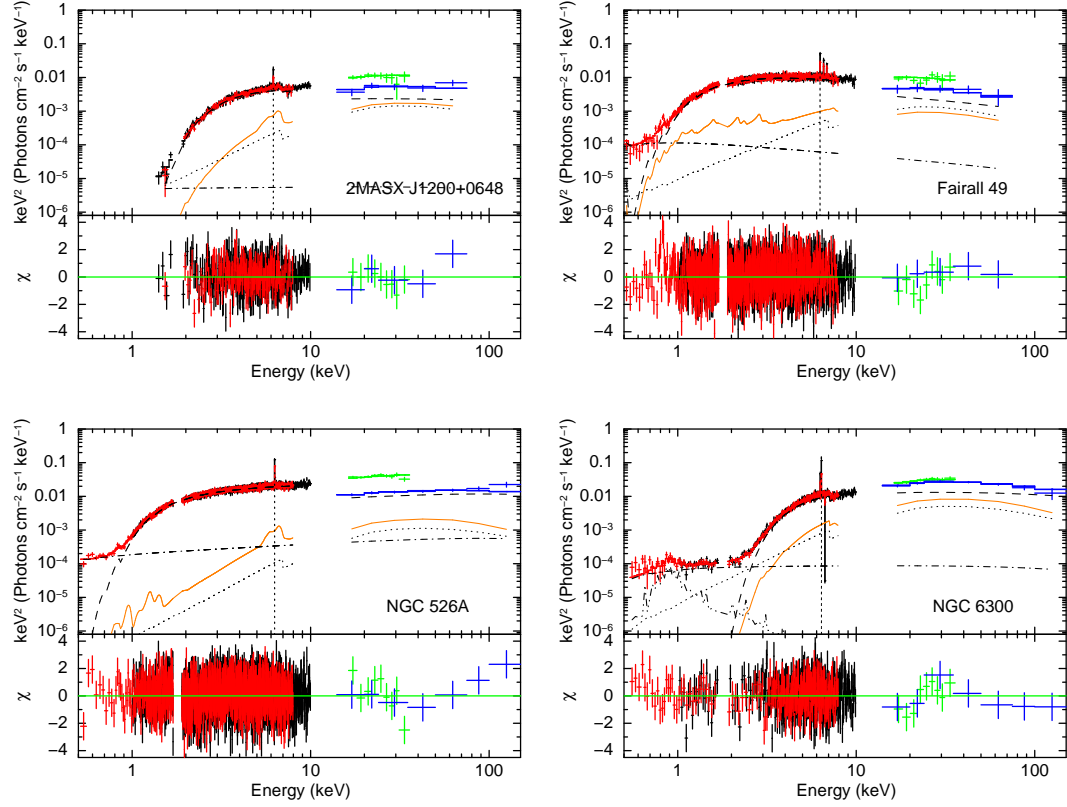


FIG. C.— Unfolded spectra and best-fitting models obtained in Section 3.2. The symbols and colors are the same as in Figure A but for the disk component represented with the orange solid line.

TABLE D
 DISK PARAMETERS

Target Name (1)	r_{in} (2)	R_{Disk} (3)	$-\Delta\chi^2$ (4)
2MASX J0216+5126	$100_{-99}^{+99}/100_{-99}^{+99}$	$0.00^{+0.15}/0.00^{+0.09}$	0.0/0.0
2MASX J0248+2630	$1_{-99}^{+99}/1_{-99}^{+99}$	$0.40^{+0.57}_{-0.40}/0.04^{+0.27}_{-0.04}$	0.1/0.0
2MASX J0318+6829	$10_{-5}^{+22}/10_{-6}^{+23}$	$0.62^{+0.32}_{-0.46}/0.55^{+0.16}_{-0.42}$	1.7/1.6
2MASX J0350-5018	$100_{-99}^{+99}/100_{-99}^{+99}$	$0.0^{+1.0}/0.0^{+1.0}$	0.0/0.0
2MASX J0444+2813	$25_{-8}^{+19}/25_{-9}^{+19}$	$1.00_{-0.27}^{+0.27}/1.00_{-0.26}^{+0.26}$	5.3/5.7
2MASX J0505-2351	$33_{-32}^{+67}/35_{-34}^{+65}$	$0.12_{-0.12}^{+0.05}/0.00^{+0.20}$	0.6/0.0
2MASX J0911+4528	$100_{-61}^{+61}/100_{-99}^{+99}$	$0.22_{-0.17}^{+0.19}/0.22_{-0.22}^{+0.35}$	1.6/0.7
2MASX J1200+0648	$29_{-10}^{+24}/20_{-5}^{+23}$	$0.62_{-0.19}^{+0.18}/0.51_{-0.10}^{+0.13}$	19.1/13.0
Ark 347	$1_{-99}^{+99}/1_{-99}^{+99}$	$0.00^{+0.54}/0.0^{+1.0}$	0.0/0.0
ESO 103-035	$4_{-2}^{+3}/4_{-2}^{+3}$	$0.17_{-0.03}^{+0.08}/0.25_{-0.07}^{+0.09}$	5.8/5.7
ESO 263-G013	$3_{-2}^{+97}/3_{-2}^{+97}$	$0.13_{-0.13}^{+0.50}/0.12_{-0.12}^{+0.52}$	0.4/0.4
ESO 297-G018	$63_{-35}^{+37}/64_{-42}^{+36}$	$0.58_{-0.40}^{+0.42}/0.48_{-0.37}^{+0.52}$	2.4/1.8
ESO 506-G027	$100_{-99}^{+99}/100_{-99}^{+99}$	$0.00^{+0.32}/0.00^{+0.27}$	0.0/0.0
Fairall 49	$30_{-17}^{+70}/4_{-2}^{+2}$	$0.11_{-0.10}^{+0.09}/0.30_{-0.06}^{+0.08}$	1.0/23.2
Fairall 51	$100_{-56}^{+56}/20_{-7}^{+14}$	$0.25_{-0.09}^{+0.12}/0.34_{-0.14}^{+0.12}$	7.5/5.3
IC 4518A	$16_{-5}^{+4}/16_{-5}^{+17}$	$0.89_{-0.36}^{+0.11}/0.99_{-0.43}^{+0.01}$	6.5/5.1
LEDA 170194	$20_{-23}^{+74}/92_{-91}^{+8}$	$0.00_{-0.00}^{+0.09}/0.00_{-0.15}^{+0.15}$	0.0/0.0
MCG +04-48-002	$1_{-99}^{+99}/1_{-99}^{+99}$	$0.0^{+1.0}/0.27_{-0.27}^{+0.73}$	0.0/0.0
MCG -01-05-047	$25_{-9}^{+36}/25_{-23}^{+75}$	$1.00_{-0.58}^{+0.25}/1.00_{-0.47}^{+0.25}$	3.0/3.0
MCG -02-08-014	$20_{-9}^{+80}/25_{-10}^{+75}$	$0.53_{-0.33}^{+0.34}/0.89_{-0.41}^{+0.11}$	3.1/6.5
MCG -05-23-016	$100_{-36}^{+36}/4_{-3}^{+2}$	$0.07 \pm 0.04/0.03 \pm 0.01$	3.7/0.9
Mrk 1210	$10_{-5}^{+15}/16_{-9}^{+16}$	$1.00_{-0.39}^{+0.10}/1.00_{-0.21}^{+0.10}$	7.1/9.0
Mrk 1498	$2 \pm 1/2_{-1}^{+2}$	$0.96_{-0.38}^{+0.04}/1.00_{-0.44}^{+0.04}$	6.5/6.3
Mrk 18	$100_{-99}^{+99}/100_{-99}^{+99}$	$0.00_{-0.00}^{+0.47}/0.00_{-0.58}^{+0.58}$	0.0/0.0
Mrk 348	$77_{-76}^{+23}/18_{-17}^{+82}$	$0.00_{-0.00}^{+0.06}/0.00_{-0.06}^{+0.06}$	0.1/0.1
Mrk 417	$1_{-99}^{+99}/3_{-2}^{+97}$	$0.00_{-0.00}^{+0.61}/0.00_{-0.00}^{+0.45}$	0.0/0.0
Mrk 520	$46_{-45}^{+54}/30_{-29}^{+70}$	$0.02_{-0.02}^{+0.27}/0.00_{-0.00}^{+0.14}$	0.1/0.0
Mrk 915	$100_{-99}^{+99}/100_{-99}^{+99}$	$0.03_{-0.03}^{+0.53}/0.04_{-0.04}^{+0.56}$	0.0/0.0
NGC 1052	$100_{-37}^{+37}/100_{-100}^{+100}$	$0.39_{-0.17}^{+0.20}/0.32_{-0.32}^{+0.32}$	4.3/2.7
NGC 1142	$70_{-69}^{+30}/28_{-27}^{+72}$	$0.00_{-0.00}^{+0.35}/0.00_{-0.16}^{+0.16}$	0.0/0.0
NGC 2110	$25_{-15}^{+75}/1_{-6}^{+6}$	$0.05_{-0.02}^{+0.03}/0.08 \pm 0.04$	1.1/1.3
NGC 235A	$11_{-10}^{+31}/1_{-1}^{+99}$	$0.86_{-0.72}^{+0.14}/0.73_{-0.65}^{+0.27}$	1.5/1.3
NGC 3081	$100_{-87}^{+87}/100_{-88}^{+88}$	$0.57_{-0.30}^{+0.43}/0.63_{-0.32}^{+0.37}$	4.1/4.2
NGC 3431	$25_{-13}^{+19}/7_{-6}^{+5}$	$0.66_{-0.35}^{+0.32}/1.00_{-0.28}^{+0.28}$	2.5/5.6
NGC 4388	$100_{-99}^{+99}/100_{-99}^{+99}$	$0.00_{-0.00}^{+0.03}/0.00_{-0.03}^{+0.03}$	0.0/0.0
NGC 4507	$1_{-6}^{+6}/100_{-32}^{+32}$	$0.59_{-0.23}^{+0.28}/0.28_{-0.15}^{+0.18}$	8.8/3.9
NGC 4992	$65_{-21}^{+35}/65_{-21}^{+35}$	$1.00_{-0.20}^{+0.20}/1.00_{-0.20}^{+0.20}$	8.4/8.2
NGC 5252	$5_{-4}^{+95}/40_{-39}^{+60}$	$0.00_{-0.00}^{+0.08}/0.00_{-0.06}^{+0.06}$	0.0/0.0
NGC 526A	$44_{-11}^{+33}/33_{-32}^{+67}$	$0.26_{-0.03}^{+0.07}/0.00^{+0.05}$	9.3/0.0
NGC 5506	$100_{-36}^{+36}/100_{-99}^{+99}$	$0.08_{-0.04}^{+0.06}/0.00_{-0.01}^{+0.01}$	5.1/0.0
NGC 6300	$2_{-1}^{+2}/2_{-1}^{+2}$	$0.39 \pm 0.11/0.56 \pm 0.16$	9.7/13.7
NGC 7172	$100_{-36}^{+36}/100_{-83}^{+83}$	$0.10_{-0.02}^{+0.03}/0.07 \pm 0.06$	3.5/1.1
NGC 788	$3_{-2}^{+97}/3_{-2}^{+97}$	$0.21_{-0.21}^{+0.55}/0.19_{-0.19}^{+0.57}$	0.2/0.1
UGC 03142	$44_{-43}^{+56}/32_{-31}^{+68}$	$0.54_{-0.54}^{+0.46}/0.55_{-0.55}^{+0.45}$	0.9/0.7
UGC 12741	$100_{-49}^{+49}/100_{-99}^{+99}$	$0.49_{-0.42}^{+0.51}/0.46_{-0.46}^{+0.54}$	1.4/1.0

NOTE. — (1) Galaxy name. (2) Inner radius in units of r_g for the assumed ionization parameters, $\xi = 10$ and 100. (3) Equivalent reflection strength for the same ionization parameters as (2). (4) Difference of the chi-squared value before and after adding the disk components for the same ionization parameters as (2). AGNs for which fitting results are significantly improved by inclusion of the relativistic reflection components from a disk are represented in boldface.

TABLE E
 INFORMATION OF HYDROGEN COLUMN DENSITY

Target Name (1)	N_{H} (2)	Obs. date (3)	Observatory (4)	Ref. N_{H} (5)
2MASX J0216+5126	$1.74^{+0.06}_{-0.07}$	2006-01-24	<i>XMM-Newton</i>	1
2MASX J0318+6829	< 14	2006-01-29	<i>XMM-Newton</i>	1
2MASX J0505-2351	9.90 ± 0.30	2009-08-06	<i>XMM-Newton</i>	2
2MASX J0911+4528	48^{+28}_{-25}	2006-04-10	<i>XMM-Newton</i>	1
2MASX J1200+0648	$10.60^{+1.01}_{-0.80}$	2006-06-26	<i>XMM-Newton</i>	1
Ark 347	$19.2^{+4.4}_{-3.5}$	2003-01-02	<i>XMM-Newton</i>	3
ESO 103-035	$18.9^{+0.6}_{-1.1}$	2002-03-15	<i>XMM-Newton</i>	4
ESO 263-G013	$25.7^{+1.5}_{-1.4}$	2007-06-14	<i>XMM-Newton</i>	4
ESO 506-G027	$66.0^{+5.0}_{-4.8}$	2006-01-24	<i>XMM-Newton</i>	3
Fairall 49	1.08 ± 0.02	2001-03-05	<i>XMM-Newton</i>	5
	1.06 ± 0.02	2001-03-06	<i>XMM-Newton</i>	5
	1.46 ± 0.01	2013-09-04	<i>XMM-Newton</i>	6
	$1.29^{+0.01}_{-0.02}$	2013-10-15	<i>XMM-Newton</i>	6
Fairall 51	$3.43^{+0.29}_{-0.31}$	2013-09-05	<i>Suzaku</i>	this work
	$4.49^{+0.49}_{-0.49}$	2013-09-07	<i>Suzaku</i>	this work
	$2.67^{+0.09}_{-0.99}$	2013-09-13	<i>Suzaku</i>	this work
IC 4518A	$14.0^{+3.0}_{-1.0}$	2006-08-07	<i>XMM-Newton</i>	4
LEDA 170194	$2.9^{+1.3}_{-0.3}$	2005-07-25	<i>Chandra</i>	4
MCG +04-48-002	$57.4^{+9.6}_{-6.6}$	2006-04-23	<i>XMM-Newton</i>	4
MCG -01-05-047	26.3 ± 1.0	2009-07-24	<i>XMM-Newton</i>	7
MCG -05-23-016	$1.25^{+0.29}_{-0.18}$	2000-11-14	<i>Chandra</i>	8
	$1.94^{+0.38}_{-0.40}$	2001-05-13	<i>XMM-Newton</i>	8
	1.80 ± 0.23	2001-12-01	<i>XMM-Newton</i>	8
	1.49 ± 0.01	2013-06-01	<i>Suzaku</i>	this work
	1.50 ± 0.01	2013-06-05	<i>Suzaku</i>	this work
Mrk 1210	$17.8^{+7.8}_{-7.9}$	2001-05-05	<i>XMM-Newton</i>	9
	$29.6^{+1.8}_{-1.7}$	2008-02-15	<i>Chandra</i>	10
	$25.5^{+3.3}_{-2.9}$	2008-02-17	<i>Chandra</i>	10
	$37.6^{+4.4}_{-4.6}$	2008-03-06	<i>Chandra</i>	10
Mrk 18	$18.3^{+7.2}_{-5.7}$	2006-03-23	<i>XMM-Newton</i>	1
Mrk 348	$13.4^{+0.20}_{-0.46}$	2002-07-18	<i>XMM-Newton</i>	11
	12.9 ± 1.2	2013-01-04	<i>XMM-Newton</i>	11
Mrk 417	54^{+25}_{-11}	2006-06-15	<i>XMM-Newton</i>	1
NGC 1052	$13.8^{+2.0}_{-1.8}$	2001-08-15	<i>XMM-Newton</i>	12
	5.3 ± 1.5	2005-09-18	<i>Chandra</i>	12
	$9.30^{+0.52}_{-0.51}$	2006-01-12	<i>XMM-Newton</i>	12
	$8.96^{+0.43}_{-0.42}$	2009-01-14	<i>XMM-Newton</i>	12
	$9.47^{+0.39}_{-0.38}$	2009-08-12	<i>XMM-Newton</i>	12
NGC 1142	$47.0^{+3.5}_{-2.9}$	2006-01-28	<i>XMM-Newton</i>	13
	$73.9^{+2.2}_{-7.0}$	2007-07-21	<i>Suzaku</i>	this work
NGC 2110	4.0 ± 1.8	2001-12-19	<i>Chandra</i>	14
	< 4.5	2003-03-05	<i>Chandra</i>	14
	3.90 ± 0.4	2003-03-05	<i>XMM-Newton</i>	14
	2.53 ± 0.13	2012-08-31	<i>Suzaku</i>	this work
	4.0 ± 0.4	2012-10-05	<i>NuSTAR</i>	14
	4.0 ± 0.7	2013-02-14	<i>NuSTAR</i>	14
NGC 4388	$25.6^{+3.1}_{-2.9}$	2001-06-08	<i>Chandra</i>	13
	$24.3^{+1.1}_{-1.0}$	2002-12-12	<i>XMM-Newton</i>	13
NGC 4507	$42.8^{+0.9}_{-0.7}$	2001-01-04	<i>XMM-Newton</i>	3
	90 ± 10	2005-07-25	<i>Chandra</i>	15
	$68.5^{+14.9}_{-9.6}$	2006-06-27	<i>XMM-Newton</i>	1
	87^{+7}_{-8}	2010-06-24	<i>XMM-Newton</i>	16
	97 ± 9	2010-07-03	<i>XMM-Newton</i>	16
	76^{+10}_{-13}	2010-07-13	<i>XMM-Newton</i>	16
	94 ± 11	2010-07-23	<i>XMM-Newton</i>	16
	80^{+8}_{-6}	2010-08-03	<i>XMM-Newton</i>	16
	65 ± 7	2010-12-02	<i>Chandra</i>	16
NGC 5252	$2.32^{+0.13}_{-0.15}$	2003-08-11	<i>Chandra</i>	17
NGC 526A	1.14 ± 0.26	2003-06-21	<i>XMM-Newton</i>	18
NGC 5506	$2.69^{+0.02}_{-0.03}$	2004-07-11	<i>XMM-Newton</i>	13
	$2.80^{+0.01}_{-0.02}$	2004-08-07	<i>XMM-Newton</i>	13
	3.09 ± 0.03	2006-08-08	<i>Suzaku</i>	this work
	3.16 ± 0.03	2007-01-31	<i>Suzaku</i>	this work
NGC 6300	$25.4^{+4.3}_{-3.7}$	2001-03-02	<i>XMM-Newton</i>	11
	$14.1^{+1.3}_{-2.0}$	2009-06-10	<i>Chandra</i>	11
	$19.8^{+1.4}_{-2.7}$	2009-06-14	<i>Chandra</i>	11
NGC 7172	$8.45^{+0.36}_{-0.33}$	2002-11-18	<i>XMM-Newton</i>	11
	8.75 ± 0.27	2004-11-11	<i>XMM-Newton</i>	11
	$8.34^{+0.16}_{-0.15}$	2007-04-24	<i>XMM-Newton</i>	11
NGC 788	$44.4^{+8.7}_{-7.8}$	2009-09-06	<i>Chandra</i>	11
	$50.3^{+6.1}_{-5.7}$	2010-01-15	<i>XMM-Newton</i>	11

NOTE. — (1) Galaxy name. (2) Hydrogen column density of the neutral full-covering absorption model. Errors correspond to the 90% confidence interval. The confidence level of the errors compiled from Hernández-García et al. (2014), Hernández-García et al. (2015), LaMassa et al. (2012), and Sazonov et al. (2005), is not clear because it is not described. (3) Observation date. (4) Observatory. (5) References for N_{H} .

References. (1) Winter et al. (2008). (2) Vasudevan et al. (2013). (3) Noguchi et al. (2009). (4) de Rosa et al. (2012). (5) Tripathi et al. (2013). (6) Lobban & Vaughan (2014). (7) Trippet et al. (2011). (8) Balestra et al. (2004). (9) Awaki et al. (2006). (10) Risaliti et al. (2010). (11) Hernández-García et al. (2015). (12) Hernández-García et al. (2014). (13) LaMassa et al. (2012). (14) Marinucci et al. (2015). (15) Sazonov et al. (2005). (16) Marinucci et al. (2013). (17) Dadina et al. (2010). (18) Brightman & Nandra (2011).